

**HURRICANE WIND RETRIEVAL ALGORITHM DEVELOPMENT FOR
AN AIRBORNE CONICAL SCANNING SCATTEROMETER**

by

SANTHOSH VASUDEVAN
B.E. University of Madras, 2004

A thesis submitted in partial fulfillment of the requirements
for the degree of Master of Science
in the School of Electrical Engineering and Computer Science
in the College of Engineering and Computer Science
at the University of Central Florida
Orlando, Florida

Fall Term
2006

ABSTRACT

Reliable ocean wind vector measurements can be obtained using active microwave remote sensing (scatterometry) techniques. With the increase in the number of severe hurricanes making landfall in the United States, there is increased emphasis on operational monitoring of hurricane winds from aircraft. This thesis presents a data processing algorithm to provide real-time hurricane wind vector retrievals (wind speed and direction) from conically scanning airborne microwave scatterometer measurements of ocean surface backscatter. The algorithm is developed to best suit the specifications for the National Oceanic and Atmospheric Administration (NOAA) Hurricane Research Division's airborne scatterometer – Integrated Wind and Rain Airborne Profiler (IWRAP). Based on previous scatterometer wind retrieval methodologies, the main focus of the work is to achieve rapid data processing to provide real-time measurements to the NOAA Hurricane Center. A detailed description is presented of special techniques used.

Because IWRAP flight data were not available at the time of this development, the wind retrieval performance was evaluated using a Monte Carlo simulation, whereby radar backscatter measurements were simulated with instrument and geophysical noise and then used to infer the surface wind conditions in a simulated (numerical weather model) hurricane wind field.

ACKNOWLEDGMENTS

I would like to thank my parents, family and all of those who have supported me throughout the years while I worked on this thesis

I would like to express my sincere gratitude to my advisor and committee chair Dr. Linwood Jones for providing me with the opportunity to work on this thesis. I am greatly indebted to him for all the countless hours he spent guiding and supporting me throughout this project.

I would also like to thank all my colleagues at Central Florida Remote Sensing Laboratory (CFRSL) and Mr. James Johnson, for their suggestions and support.

Last but not least, I would like to say thank you to my committee members including, Dr. Takis Kasparis, and Dr. Stephen Watson for their time and guidance.

This work was sponsored under a grant from NASA Headquarters ESSD to support the Ocean Vector Winds Science Team activities.

TABLE OF CONTENTS

LIST OF FIGURES	v
LIST OF TABLES	vii
LIST OF ACRONYMS	viii
CHAPTER 1: INTRODUCTION	1
1.1 Objective	1
1.2 Introduction to Scatterometry	1
1.3 Ocean Surface Backscatter	3
1.4 History of scatterometry	7
CHAPTER 2: MICROWAVE SCATTEROMETERS	10
2.1 Instrument description and characteristics	10
2.2 IWRAP instrument description	14
CHAPTER 3: ANALYSIS OF WIND VECTOR CELLS	20
3.1 Wind vector cell definition	20
3.2 Design of wind vector cell collocation algorithm	22
3.3 Effects of attitude variations	28
4.1 Background of Wind Vector Retrieval	33
4.2 Geophysical Model Function	34
4.3 Design and Testing of Wind Retrieval Algorithm	42
4.3.1 Maximum Likelihood Estimator	42
4.3.2 Compass Simulation	48
5.1 Simulation of aircraft over-flight	52
5.1.1 Hurricane wind field simulation	52
5.1.2 Simulated radar measurements	54
5.2 Results from Simulation	58
CHAPTER 6: CONCLUSIONS	64
APPENDIX	65
LIST OF REFERENCES	77

LIST OF FIGURES

Figure 1.1 Specular reflection from ocean surface.	3
Figure 1.2 Representation of a rough surface as a collection of facets.....	4
Figure 1.3 Bragg resonant scattering from ocean waves.	5
Figure 1.4 Bragg scattering from short waves tilted by long waves.....	6
Figure 2.1 Cross track scanning radar geometry.	10
Figure 2.2 Conical scan radar geometry.	11
Figure 2.3 Scatterometer instantaneous field of view.....	13
Figure 2.4 Conical scanning radar footprint.	14
Figure 2.5 IWRAP: conical scanning radar	15
Figure 2.6 General diagram of IWRAP system.....	16
Figure 2.7 Azimuth binning of each antenna revolution.	18
Figure 3.1 Wind vector cells and scanning geometry.....	21
Figure 3.2 Airborne radar measurement geometry.	23
Figure 3.4 Effect of 0 deg roll -2 deg pitch variation on scan contour.	29
Figure 3.5 Effect of +2 deg roll 0 deg pitch variation on scan contour.	29
Figure 3.6 Effect of 0 deg roll +2 deg pitch variation on scan contour.	30
Figure 3.7 Effect of +2 deg roll 0 deg pitch variation on scan contour.	30
Figure 3.8 Effect of +2 deg roll +2 deg pitch variation on scan contour.....	31
Figure 3.9 Effect of -2 deg roll -2 deg pitch variation on scan contour.....	31

Figure 4.1 Response of GMF at various wind speeds for C band.	40
Figure 4.2 Response of GMF at various wind speeds for Ku band.	41
Figure 4.3 Best wind vector solution occurs at “tightest” intersection of four curves.	44
Figure 4.4 Isotropic Sigma-0 at C band V-pol for 40 deg incidence.	46
Figure 4.5 Cost Surface for wind direction range of 360 deg and wind speed ± 4 m/s.	47
Figure 4.6 Cost surface: calculated at ± 60 deg of flight level wind direction and wind speed ± 4 m/s.	47
Figure 4. 7 Typical compass testing cases.	49
Figure 4 8 Compass testing: difference between retrieved and true wind speed and direction.	51
Figure 5.1 Simulated hurricane wind field with noise added.	53
Figure 5.2 Antenna footprint center locations during conical scans.	55
Figure 5.3 Wind direction bias added to simulate flight level wind direction measurement.	57
Figure 5.4 Monte Carlo simulated results for hurricane Floyd.	59
Figure 5.5 Analysis of pixel by pixel error in simulated hurricane.	60
Figure 5.6 Scatter plot of wind speeds.	62
Figure 5.7 Scatter plot of wind directions.	63

LIST OF TABLES

Table 3. 1 Assignment of sigma-0 measurements to WVC's for (a) 30 deg and (b) 40 deg beams.	25
Table 3. 2 Location of sigma-0 measurements from multiple scans.	26
Table 3.3 Number of independent azimuth binned measurements.	27
Table 4.1 Values of coefficients β , γ_1 , and γ_3	36
Table 4. 2 Saturation wind speed values.....	36
Table 4.3 Coefficients for eq 4.5	38
Table 4. 4 Coefficients for eq 4.6	38
Table 5.1 Sample of output serial data record.	56

LIST OF ACRONYMS

NRCS	Normalized radar cross section (σ_0)
V	Vertical
H	Horizontal
EM	Electromagnetic
CW	Continuous wave
NASA	National Aeronautics and Space Administration
IFOV	Instantaneous field of view
ESA	European space agency
GMF	Geophysical model function
TC	Tropical cyclone
ABL	Atmospheric boundary layer
PRF	Pulse repetition frequency
RF	Radio frequency
DAS	Digital acquisition system
WVC	Wind vector cell
NOAA	National Oceanic and Atmospheric Administration
HRD	Hurricane research division
IF	Intermediate frequency

CHAPTER 1: INTRODUCTION

1.1 Objective

The objective of this thesis work is to develop a data processing algorithm based upon previous scatterometer wind retrieval methodologies. The algorithm is designed for application to a new class of airborne, dual-frequency, conical scanning, microwave radar scatterometers, which will provide near real-time wind vector retrievals with minimum auxiliary information that would be available from aircraft systems.

1.2 Introduction to Scatterometry

RADAR (Radio Detection And Ranging) is a system that transmits radio waves in a pulsed or continuous fashion and measures the reflected power and/or frequency from a remote object (target), which is analyzed to determine the characteristics of the object. There are numerous civil and military applications for the RADAR such as air traffic control; target detection and tracking, and weather monitoring. A scatterometer is a special purpose radar sensor that makes a quantitative measurement of electromagnetic (EM) scattering from the earth's surface. For our purposes, we are concerned with radio waves transmitted to the ocean surface by a downward looking satellite/air-borne radar. The EM energy is scattered into many different directions after striking the sea and a small portion of this scattered energy, carrying with information about phenomena at sea surface, is eventually received by the radar. This reflected energy can be measured and used to infer the ocean surface wind vector.

For a "point" target, the relationship between the power transmitted P_t and power received P_r by a long pulse or CW radar is given by the mono-static radar equation:

$$P_r = \frac{P_t G^2 \lambda^2}{(4\pi^3) R^4} \sigma, \text{ Watts} \quad (1.1)$$

where,

P_t = Power transmitted by the radar, W

G = Gain of the radar antenna

λ = Wavelength of the radio wave, m

R = Distance to the target from radar, m

σ = Radar cross section of the target, m²

For a distributed radar target (such as ocean surface), the normalized radar cross section σ^0 , is the measure of the ocean surface's ability to reflect radar signals in the direction of the radar receiver, i.e. it is a measure of the ratio of backscatter power per steradian (unit solid angle) in the direction of the radar (from the target) to the power density that is intercepted by the target [1].

Normalized radar cross section or σ^0 is defined by the equation:

$$\sigma^0 = \sigma / IFOV, \text{ dimensionless} \quad (1.2)$$

where the IFOV is the instantaneous antenna field of view (or antenna footprint area on the ocean surface).

In the case of a scatterometer, power transmitted by the radar P_t is recorded, gain of the antenna and wavelength used by the radar are known, and the range or distance to the distributed surface target is known by the geometry of the measurement. Hence, all the parameters in the

radar equation (1.1) are known except the normalized radar cross section, which can thus be calculated.

Also the scatterometer can indirectly measure (infer) geophysical parameters such as the ocean wind speed and direction at the ocean surface by interpreting the measured normalized radar cross section at the surface from different azimuth look directions

1.3 Ocean Surface Backscatter

Because the penetration depth of microwave radiation in sea water is less than a few millimeters and since the dielectric properties of the sea surface are relatively uniform for a given radar measurement geometry, backscatter from the sea is dominated by surface scattering. For angles of incidence θ near normal incidence ($\theta \sim 0^\circ$), radar scattering comes from mirror like facets of the sea surface aligned so as to reflect energy directly back toward the transmitter. Figure 1.1 shows specular reflections from near normal incidence with ocean wave troughs and almost flat horizontal surfaces.

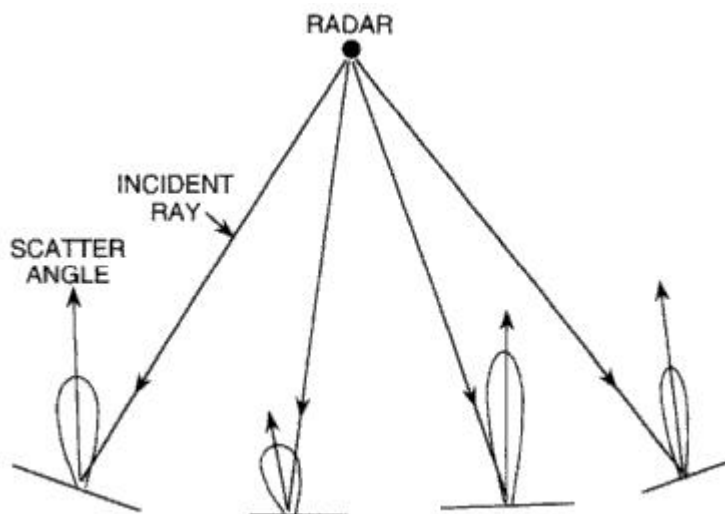


Figure 1.1 Specular reflection from ocean surface.

For an off-nadir geometry, calm seas cause specular scattering, away from the radar and therefore results in weak received echo power. On the other hand, rough seas produce higher backscatter because a rough surface can be modeled as a collection of multiple tilted facets as shown in Fig. 1.2. Since these facets are oriented at different angles, the probability of occurrence of some facets producing backscatter is higher and the received power increases with increasing surface roughness.

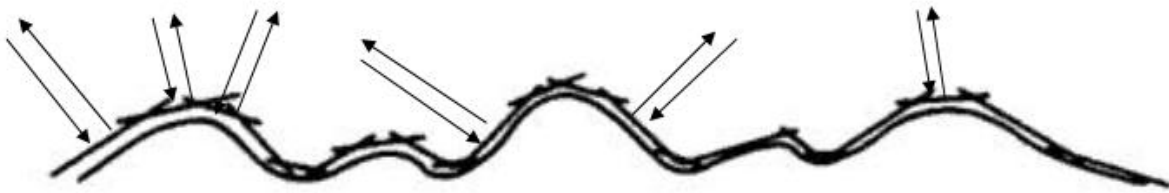


Figure 1.2 Representation of a rough surface as a collection of facets.

Since there are few wave slopes that exceed $\sim 15^\circ$, specular point scattering applies only to a small range of incidence angles near-nadir incidence. Yet ocean scattering occurs for all incidence angles, and the explanation for this phenomenon for off-nadir scattering is given by a resonant Bragg scattering theory.

The rough ocean surface can be decomposed into its sinusoidal Fourier components, and super-position can be applied for calculating the radar backscatter. Figure 1.3 depicts the Bragg scattering mechanism caused by small ocean surface waves that satisfy the Bragg resonant conditions. These short ocean waves, called capillary waves or ripples, cause the dominant reflectance of the incident radar beam for moderate to high incidence angle ($\theta > 30^\circ$) backscatter. Bragg scattering, also known as resonant scattering, is caused by a periodic collection of

scatterers (ocean waves) whose wave crest separations (wavelengths on the surface) are comparable to that of the radar electromagnetic wavelength. The Bragg resonant condition exists when there is a constructive interference of backscatter from the wave crest for a large number of periodically-spaced scatterers given as

$$\lambda_s = 2\lambda_r \sin \theta \quad (1.3)$$

where λ_r is the radar free-space wavelength

λ_s is the Bragg ocean wavelength that produces reinforcement

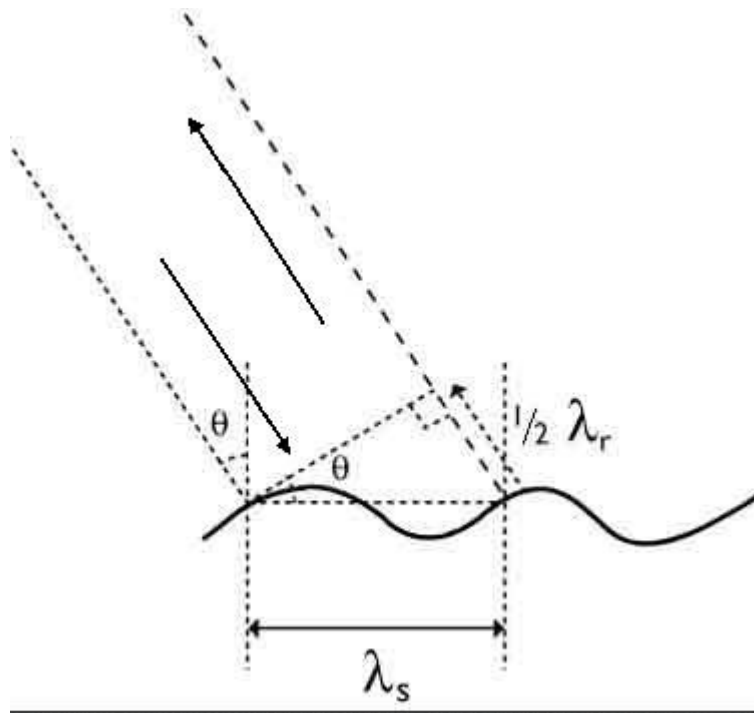


Figure 1.3 Bragg resonant scattering from ocean waves.

For example, at an incidence angle of 30° , the Bragg ocean wavelength is equal to the radar wavelength. Thus at angles well off-nadir ($> 30^\circ$), the radar acts as a spatial filter and selectively measures the roughness caused by the Bragg waves. These capillary waves have

dimensions of order 1 cm; and they reside on the structure of the larger sea state (gravity ocean waves) as shown in figure 1.4.

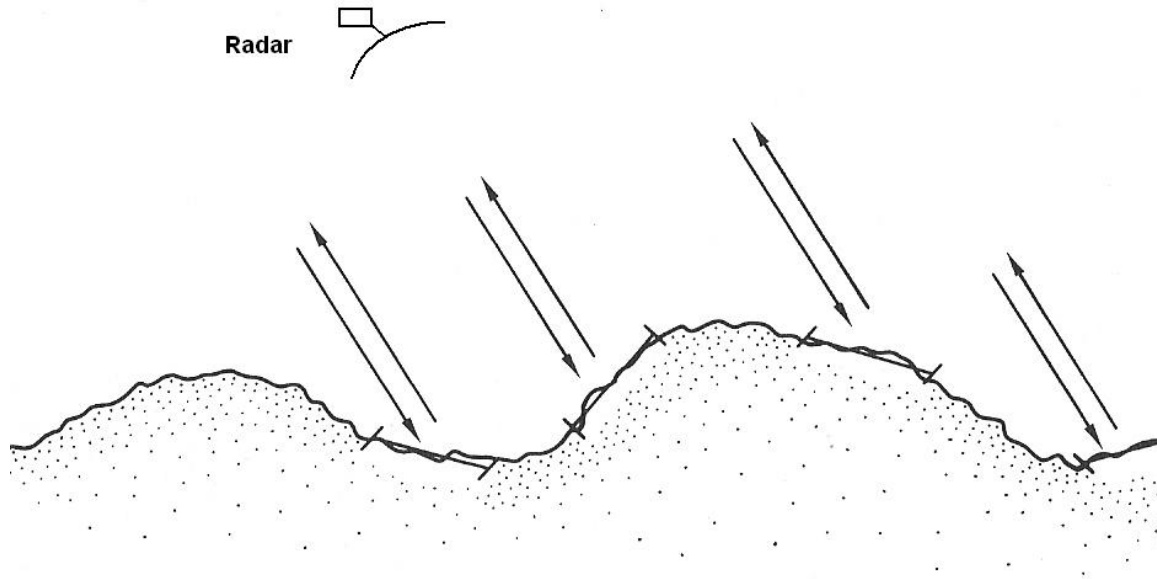


Figure 1 4 Bragg scattering from short waves tilted by long waves.

Bragg ocean waves, that are the largest contributors to ocean surface backscatter, are caused air drag (friction) of the ocean surface winds. Essentially, surface wind speed (and direction) are the principal source of modulation of these surface capillary waves, and since the backscatter is primarily from these waves, the resulting backscattered power is proportional to the instantaneous wind speed and direction averaged over the antenna footprint on the ocean's surface. Through the use of the radar equation, the ocean surface normalized cross section (σ_0) may be measured.

Also a secondary Bragg- wave modulating feature is the tilt-mechanism from long ocean waves (illustrated in Fig. 1.4), which changes the local incidence angle and causes the

normalized radar cross section to vary over the wave surface. Never the less, these modulations, which occur over scales of 10's – 100's meters, do not become a significant effect for a scatterometer backscatter measurement because the radar backscatter is averaged over the antenna footprint that are typically a few Km.

1.4 History of scatterometry

For over 30 years, microwave scatterometers on aircraft and satellites have proven their effectiveness in the measurement of ocean surface wind vector [2]. Satellite based scatterometers are effective in mapping the global ocean surface wind field on a daily basis; whereas, aircraft scatterometers play a vital role in high spatial resolution, real-time monitoring of tropical storms and hurricanes. The first space borne scatterometer flew as a part of the National Aeronautics and Space Administration's (NASA) Skylab missions in 1973 and 1974, demonstrating that space borne scatterometers were feasible. Simultaneously, one of the first airborne radiometer-scatterometer (RadScat) was developed at NASA Langley Research Center. RadScat pioneered in several novel technologies like combining a radiometer and scatterometer and the use of circular flights to measure the ocean surface sigma-0 anisotropy [3]. Since then, various satellite scatterometers like NASA's SeaSat (1978), NSCAT (1996), QuikSCAT (1998) and SeaWinds on ADEOS-2 (2002), and the European Space Agency (ESA)'s ERS-1 (1990) and -2 (1995) have proven their vital role in gathering ocean surface wind field data to understand and predict the ocean weather [4 - 6].

The radar backscatter measurements obtained at multiple azimuth looks of the surface can be interpreted to retrieve (infer) ocean surface wind speeds and directions, through the use of

a Geophysical Model Function (GMF). The GMF relates the backscattered power to wind speed and direction on the surface of the ocean. For more than three decades, physically-based [7] and empirically-based [8, 9] model functions have been developed to describe the ocean backscatter's relationship to the ocean surface wind speed and direction. Due to insufficient knowledge of the complex relationship between the sea surface roughness and environmental conditions, and the electromagnetic scattering mechanisms from rough ocean surfaces, the inversion of aircraft and spacecraft scatterometer measurements currently relies on empirically-based models rather than physically-based theoretical models. Two presently used model functions are the QuikSCAT (QSCAT1) model function at Ku-Band [10] (derived from the SeaWinds scatterometer aboard the NASA QSCAT satellite) and the CMOD5 model function at C-Band [11] (developed from the Active Microwave Instrument (AMI) sensor aboard the European Space Agency (ESA) ERS-1 and ERS-2 satellite).

Having proven its effectiveness in monitoring the ocean surface winds, the importance of scatterometers in studying Tropical Cyclones (TC's) was soon realized. *Katsaros et al.* [12] demonstrated improved skill in detecting TC development using scatterometer winds from QuikSCAT. *Isaksen and Stoffelen* [13] showed that ERS scatterometer winds had a positive impact on TC analyses and forecasts at the European Centre for Medium-Range Weather Forecasts (ECMWF). They showed the potential of C-band scatterometry to aid in monitoring and forecasting of TC's, but pointed out that the winds were underestimated within the TC due to CMOD4 [14] (which is a widely used C-band GMF) over-estimating the backscatter of the ocean surface for high wind speeds and thus underestimating high winds. *Donnelly et al.* [15] developed a new model, CMOD4HW, which incorporates this reduction in sensitivity at high

wind speeds, and these results were used in the derivation of the currently operational CMOD5 GMF [11].

New GMF's, based upon aircraft measurements in hurricanes, were presented by *Fernandez et al.* [16] at C- and Ku-band and VV polarization for wind speeds ranging from 15 to 55 m/s. These GMF's were derived from measurements acquired by the University of Massachusetts (UMass) C- and Ku-band airborne scatterometers through Hurricanes Brett (1999), Dennis (2005), and Floyd (1999). These measurements indicated a decreased sensitivity at both frequency bands above 45 m/s in order to overcome the limitation of conventional GMF's in predicting the tropical cyclone (TC) wind fields. This is the primary source of GMF used in this thesis. Chapter 4 of this thesis report goes further into the discussion of the GMF, explaining the adaptations for interpreting the high wind speeds in TC's.

CHAPTER 2: MICROWAVE SCATTEROMETERS

2.1 Instrument description and characteristics

Scatterometers are named depending on the type of scanning performed by the radar antenna. Two most common types of scanning are:

1. Cross track scanning
2. Conical scanning radar

Cross track scanning is shown in Fig. 2.1. In this type of radar, the antenna scans along a line, which is perpendicular to the ground track of the satellite/ aircraft. Because of this, there is no useful azimuth diversity in the radar backscatter and also the incidence angle constantly changes throughout the scan, which makes the data processing more complex.

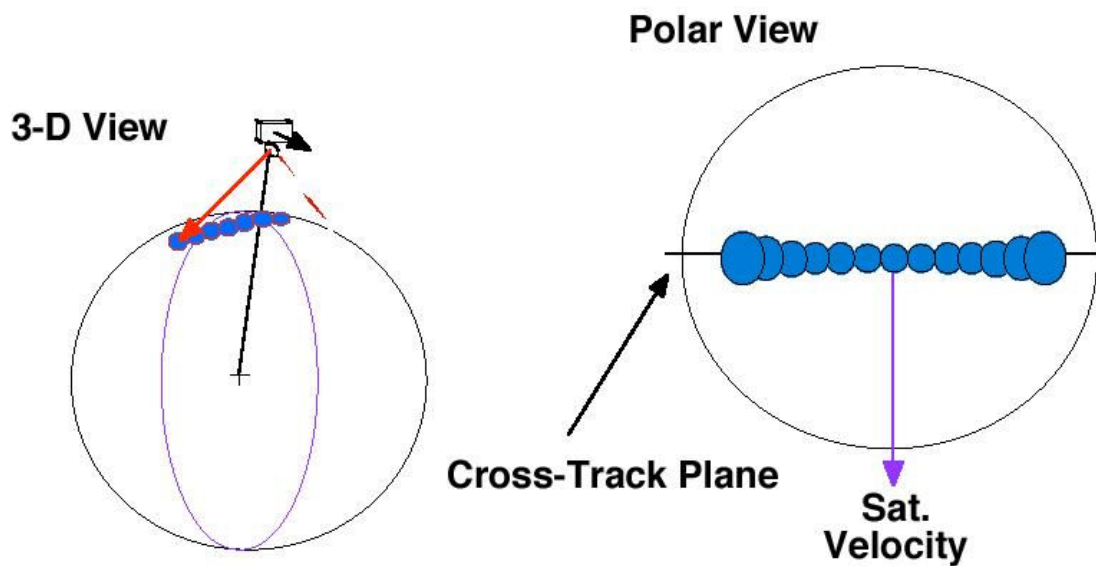


Figure 2.1 Cross track scanning radar geometry.

The most commonly used viewing configuration for microwave scatterometers is “conical scan”. For such an earth viewing instrument, the spin axis points to the center of the earth, and the incidence angle, defined by the angle between the normal to the surface and the antenna direction of propagation, remains constant as the antenna scans 360 deg in azimuth. The major advantage of this type of scatterometer is that it views a spot on the surface at two different azimuth angles (looking forward and aft) as the aircraft flies along its ground path. Figure 2.2 illustrates the geometry of a conical scanning scatterometer looking at the earth’s surface.

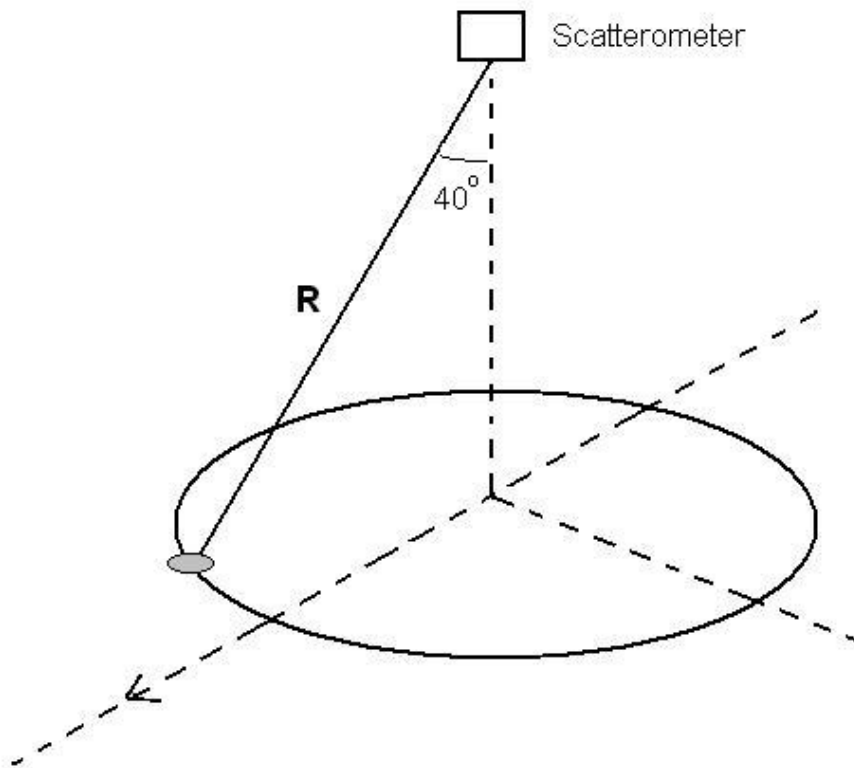


Figure 2.2 Conical scan radar geometry.

At lower altitudes, as in the case of aircraft borne scatterometers, the earth can be considered as a flat surface (plane), as opposed to a spherical surface. At low altitudes (< 3 km) considered in this thesis, this is a good approximation; thereby the effects of earth's curvature can be neglected. Thus, θ_i represents the incidence angle (and nadir angle) and is related to the slant range, R by:

$$\text{Cos } \theta_i = \frac{h}{R} \quad (2.1)$$

Where h is the altitude of the scatterometer.

Therefore the slant range R is given by the equation

$$R = \frac{h}{\text{Cos } \theta_i} \quad (2.2)$$

As the antenna scans, it makes observations of the surface over its instantaneous field of view (IFOV), which is the elliptical shape antenna footprint on the surface (as shown Fig. 2.3).

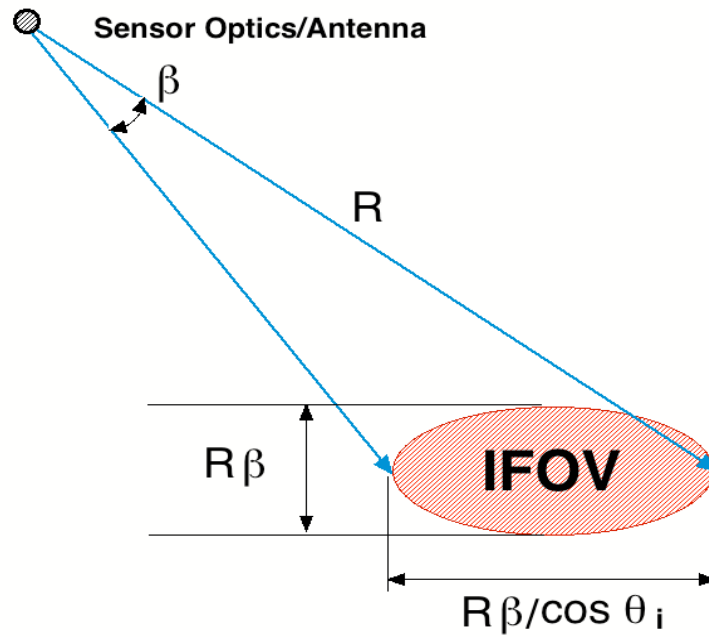


Figure 2.3 Scatterometer instantaneous field of view.

Scan rate of a conical scanning scatterometer is defined as the number of revolutions the scatterometer antenna makes in a minute. The rotational motion of the antenna combined with the forward motion of the scatterometer results in a spiral shaped locus of IFOV's as shown in Fig. 2.4. The shape of the spiral scan foot-print is determined by the scan rate and the forward velocity of the aircraft.

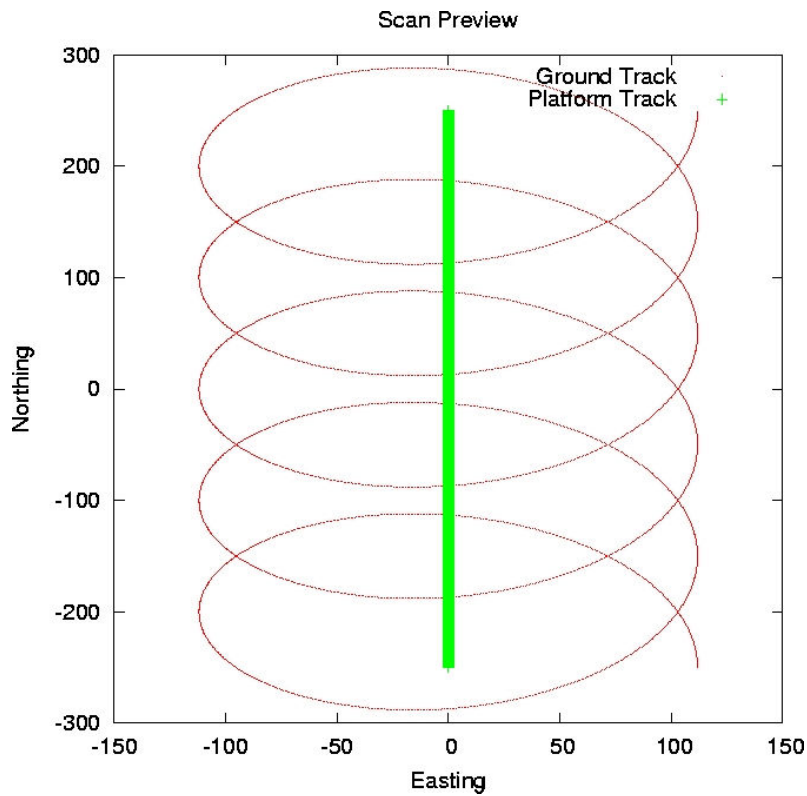


Figure 2.4 Conical scanning radar footprint.

2.2 IWRAP instrument description

The paper by D. E. Fernandez, E. M. Kerr, A. Castells, J. R. Carswell, S. J. Frasier, P. S. Chang, P. G. Black, and F. D. Marks, titled “IWRAP: the Imaging Wind and Rain Airborne Profiler for Remote Sensing of the Ocean and the Atmospheric Boundary Layer within Tropical Cyclones” [17], has been the primary source of information about the IWRAP program and the instrument description. Excerpts from the paper (given below in *italics*) have been used to provide the instrument details.

The Imaging Wind and Rain Airborne Profiler (IWRAP) is a conically scanning, dual frequency (C- and Ku-band) radar, which measures the reflectivity (backscatter) from the ocean surface at four different incidence angles, approximately 30, 35, 40 and 50 degs (see Fig. 2.5).

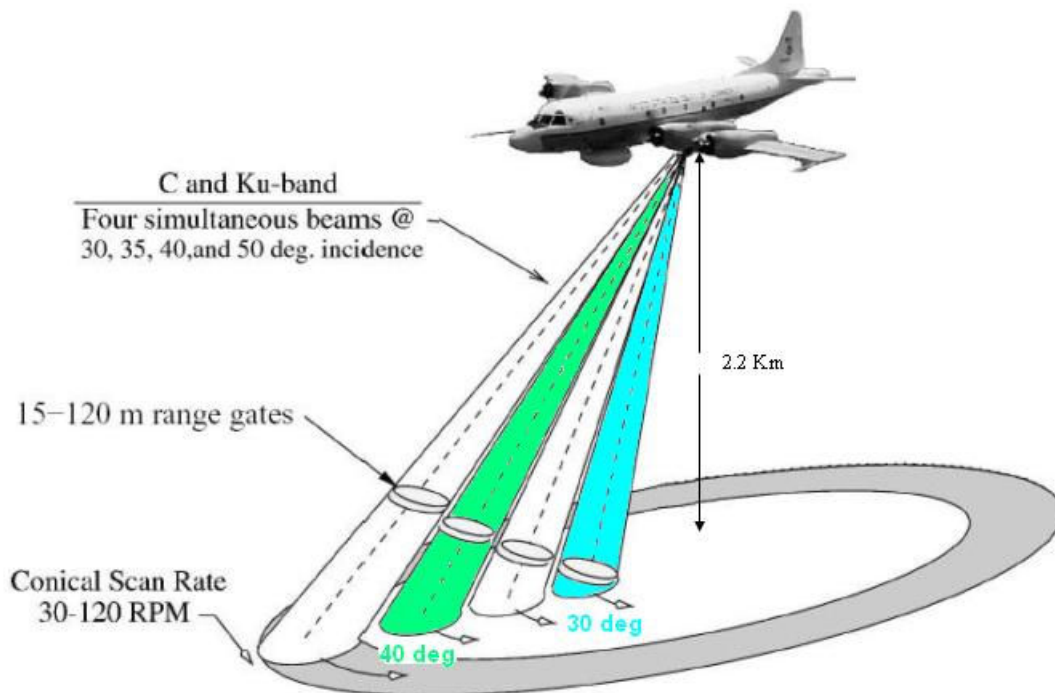


Figure 2.5 IWRAP: conical scanning radar

IWRAP measures the full azimuthal backscatter response at four incidence angles, two frequencies and two polarizations. A simplified radar block diagram is shown in Fig. 2.6. *“The slant range resolution is established by the desired resolution in the atmospheric boundary layer (ABL) wind measurements within hurricanes: low-level, high-speed wind currents can vary greatly over a small (50 - 100 m) vertical distance. The resolution must therefore be such that these variations are observable.”*

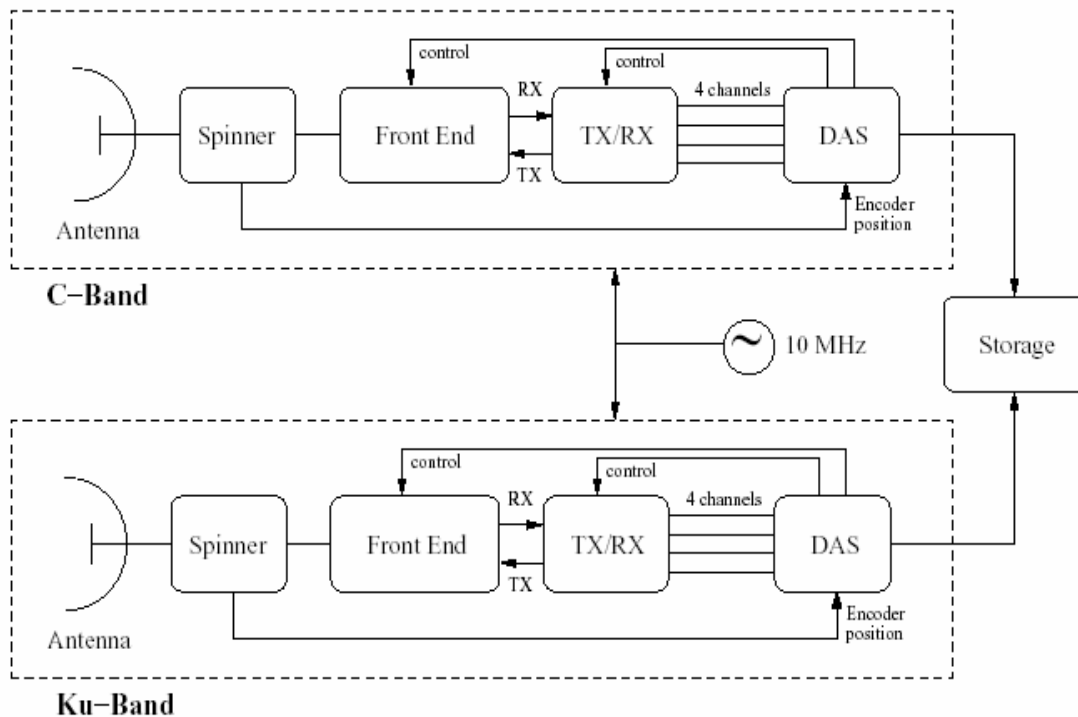


Figure 2.6 General diagram of IWRAP system

“High resolution measurements are also required to resolve the structure of meso-vortices (small scale rotational features found in the eye walls of intense tropical cyclones) which are typically 50 to 100 m in size. To satisfy these requirements, IWRAP operates with range resolutions selectable in the 15 to 120 m range. This translates into 100 ns to 800 ns pulse widths, and receiver bandwidths of 10 to 1.25 MHz, respectively. In selecting the PRF, the trade-off between unambiguous range distance and maximum Doppler velocity, as well as spatial resolution, both in range and time (i.e. fast conical scanning), need to be considered. The PRF needs to be low enough to avoid range ambiguities (at a given flying altitude), and high enough to avoid Doppler velocity ambiguities. These requirements need to consider that the measured Doppler velocity from precipitation presents two main contributions: the speed of the

hydrometeors and the motion of the aircraft. To address these requirements, IWRAP's PRF can be set between 1 kHz and 100 kHz. The conical scanning rate can be selected within the 30 to 120 RPM range. A nominal conical scanning rate of 60 RPM allows retrieving a full conical scan every second and this is the selected scan rate that is used for wind retrieval in this algorithm".

The antenna sub-system consists of two similar (C- and Ku-band) frequency-steerable micro strip patch array antennas capable of scanning through incidence angles ranging from 20 to 50 degs off boresight by sweeping the transmitted frequency from approximately 5 to 5.5 GHz at C-Band for the dual-polarized antenna (4.98 to 5.7 GHz for the single-polarized antenna), and from 12.9 to 14.2 GHz at Ku-Band (12.8 to 14.8 GHz for the single-polarized antenna). For wind vector retrieval proposes only two incidence angles, 30 and 40 degs, are used.

"The basic function of the Front end Transmit/Receive (Tx/Rx) sub-system is to generate the transmitted pulses and up-convert them to the appropriate radiofrequency (RF) frequencies, as well as to down-convert the received signal and separate it into the channels that will then be routed to the Digital Acquisition System (DAS). The front end subsystem performs the amplification of the signals to be transmitted and routes them to the antenna subsystem during transmission, and amplifies the received signal and routes it back to the Tx/Rx subsystem during reception. It also incorporates an internal calibration loop to correct for system gain drifts".

"The DAS implements a digital receiver that performs in-phase and quadrature (I&Q) demodulation on each one of the four IF output received signals provided by the Tx/Rx subsystem. These IF signals have a maximum 1 dB bandwidth of 10 MHz. The IF demodulation into complex baseband in the digital domain avoids typical gain imbalances and DC offsets associated with analog quadrature phase detectors".

The radar backscatter collected during a 360° scan is pre-averaged and binned into 32 equal bins of 11.25° each. This is illustrated in Fig. 2.7. For the purpose of wind retrieval, this algorithm makes use of two incidence angles which are 30° and 40° , shown in the figure. For each azimuth bin, the central point of the bin is taken as the point at which the measurement for that bin is made and the azimuth angle at point is taken as the discrete azimuth angle for that bin.

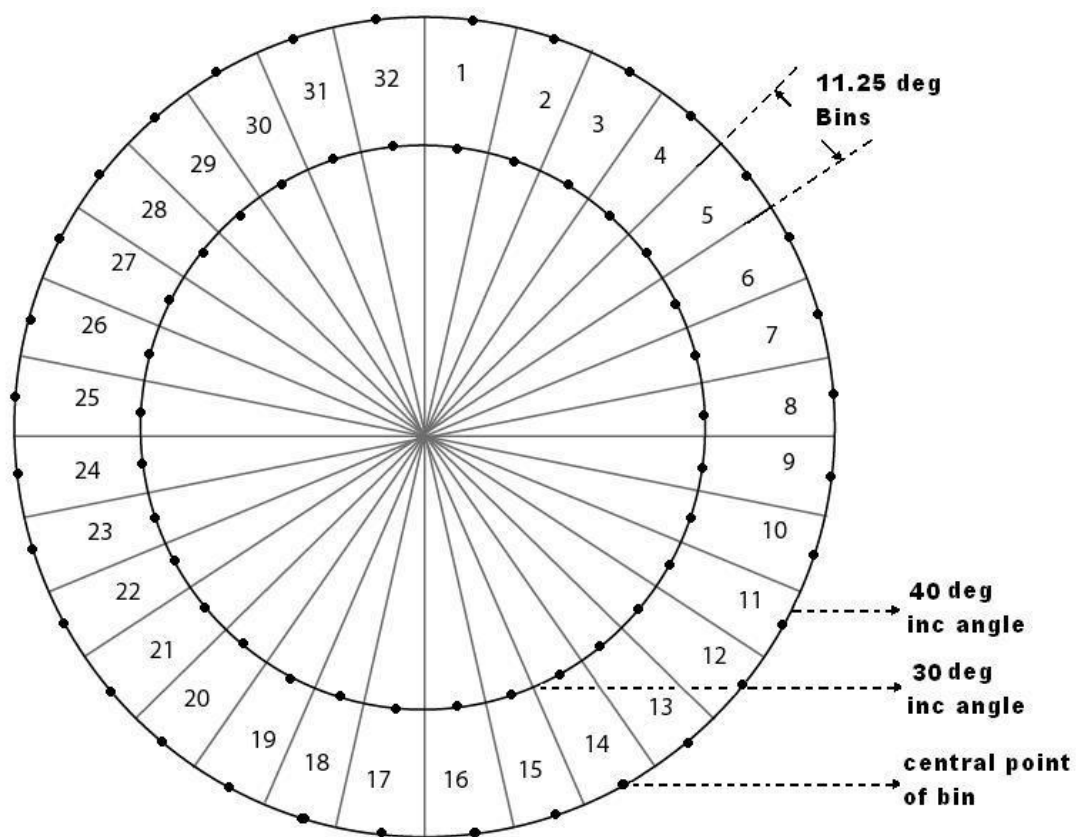


Figure 2.7 Azimuth binning of each antenna revolution.

In addition to the scatterometer data from the instrument, this algorithm utilizes the following auxiliary data from the aircraft:

- Aircraft altitude (from radar altimeter)
- Aircraft sub-point Latitude/Longitude location (from inertial navigation or GPS systems)
- Wind direction at the cruising altitude (derived from inertial navigation system).

CHAPTER 3: ANALYSIS OF WIND VECTOR CELLS

3.1 Wind vector cell definition

A wind vector cell (WVC) is the smallest unit of area in which a unique measurement of wind parameters is made, and it constitutes a single pixel on a retrieved-wind map. The WVC's form a rectangular grid (matrix), centered on the aircraft ground track, which is designated by numbers (1 through "#") for along-track rows and letters ("a" through "d") for cross-track columns. The dimensions of a wind vector cell on the ground depend on the scan geometry and the scatterometer antenna beamwidth. In the case of IWRAP, the incidence angles of the beams are 30 deg and 40 deg, and the antenna beamwidth is 6.5 deg, this results in a surface footprint of approximately 500 m. It is assumed that the aircraft flies at a nominal altitude of about 2.2 Km, and the resultant edge to edge swath width of the scanning pattern is 4 Km for the outer (40 deg) beam and 3 Km for the inner (30 deg) beam as shown in Fig. 3.1.

The figure describes the locus of boresights of the two scanning beams, as they scan over the WVC grid. The measurements along the 360 deg scan (one antenna revolution) are binned into 32 azimuth bins, and the azimuth position is taken to be mid point of the azimuth bin ($N \times 11.25 / 2 = N \times 5.625$ deg), which are shown as bold dots on the contour. This figure depicts a scenario in which the aircraft is moving from south to north. As the aircraft scans it also moves ahead simultaneously, which means that by the time the scatterometer scans from fwd to aft, the aircraft would have moved forward by a distance equal to the velocity of the aircraft times the time for half the period of the conical scan. This distance is negligibly small compared to the diameter of the scan circle; so this effect can be neglected, when analyzing the scan contour of a

singe scan. The azimuth angles relative to the flight direction thus are 5.625 deg, 16.875 deg, 28.125 deg, etc.

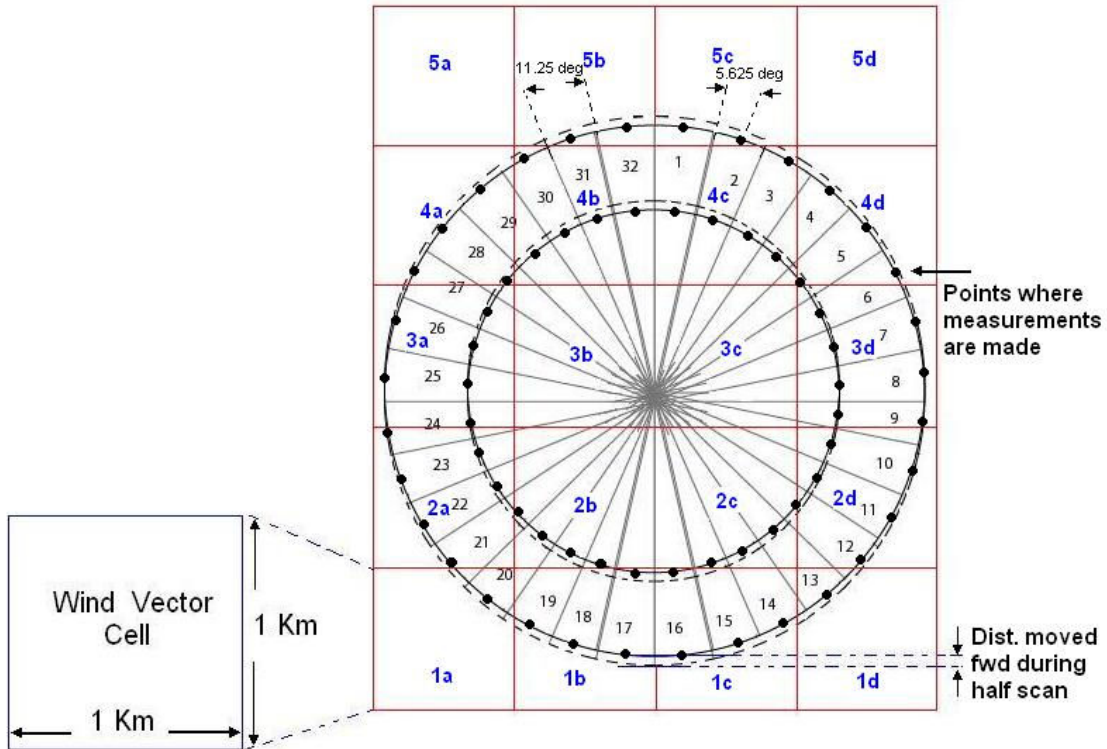


Figure 3.1 Wind vector cells and scanning geometry.

3.2 Design of wind vector cell collocation algorithm

An efficient algorithm was developed, which would collocate the sigma-0 measurements into corresponding wind vector cells as the radar scans progressively. This algorithm, along with the main retrieval algorithm, should run fast enough to facilitate real-time wind retrieval. An algorithm which uses actual IFOV center Latitude (Lat) and Longitude (Lon) values, to collocate measurements would be computationally inefficient because the process would involve multiple logical loops and comparisons to test if the radar IFOV lies within the WVC boundaries. By virtue of IWRAP's simple measurement geometry, this computationally inefficient method could be replaced with a simpler method, which involves using fixed time delays for sigma-0's along columns to collocate measurements into WVC's. An assumption is made that the aircraft cruises at a constant speed while scanning; however, a change in this speed can also be accommodated by using a different delay table, which is one of the inputs to the algorithm.

In the case of IWRAP, the aircraft cruises at speed of approximately 125m/s as it traverses through the hurricane; so it takes ~ 8 sec for the aircraft to pass over one WVC of 1 Km dimension. With a scanning rate of 60 rpm, it means that the scatterometer completes 8 scans in the time that it takes to fly over the 1 Km WVC. In-flight measurements give the aircraft altitude and the geo-location (Lat/Lon) of the sub-point directly beneath the aircraft, and the incidence angle of the beams are known. Using these data, the geo-location (Lat/Lon) of the antenna beam footprints for all azimuth bins of the first scan can be calculated as shown in Fig. 3.2.

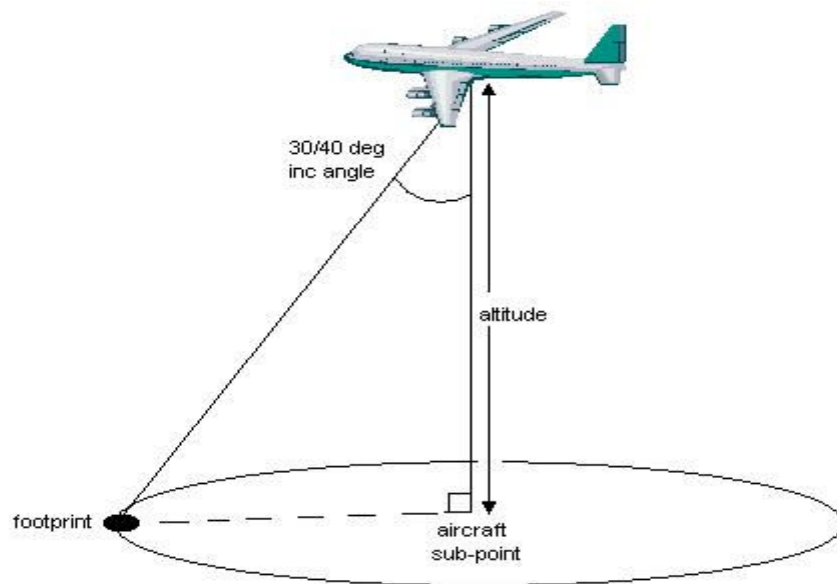


Figure 3.2 Airborne radar measurement geometry.

Once the geo-location of the footprint for the first scan is calculated for every azimuth bin, it is used as reference to map actual Lat/Lon to relative position on the WVC grid. As explained above, for eight consecutive scans, measurements fall into the next WVC along-track. Data from the scatterometer comes sequentially, starting with the sigma-0 measurement for the first azimuth bin and continues till bin # 32 for a single scan. At a scan rate of 60 RPM, the time delay between subsequent bin

The flow diagram presented in Fig. 3.3 illustrates the collocation algorithm procedure. Each sigma-0 measurement is assigned into a WVC according to its position. The assignment of an sigma-0 measurement into a WVC for the first scan is depicted in Table 3.1; and the naming convention of WVC's in the grid is shown in Fig. 3.1.

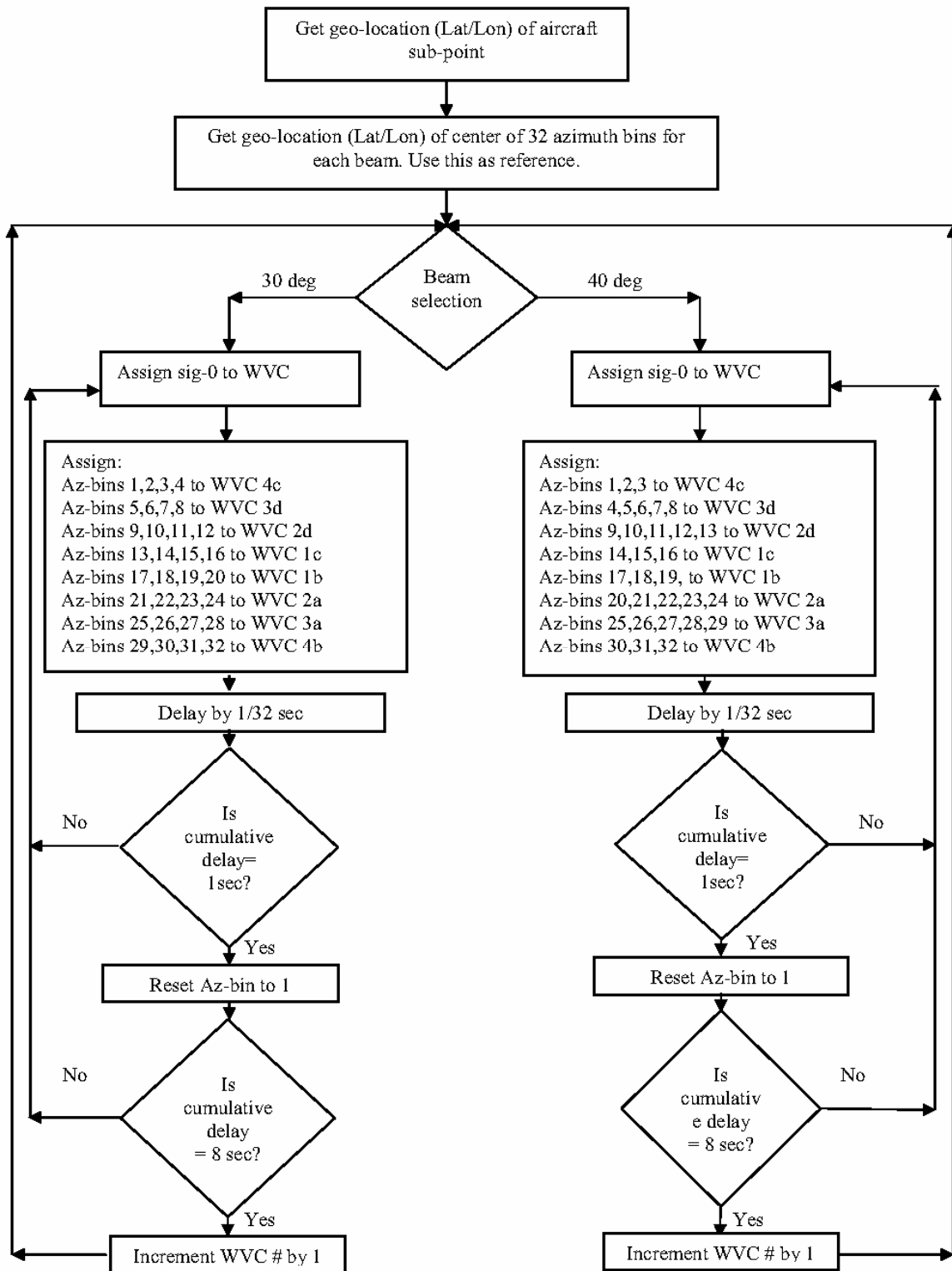


Figure 3.3 Flow diagram for WVC collocation

Table 3. 1 Assignment of sigma-0 measurements to WVC's for (a) 30 deg and (b) 40 deg beams.

(a)								
WVC	4C	3D	2D	1C	1B	2A	3A	4B
Az Bins that	1	5	9	13	17	21	25	29
go into WVC	2	6	10	14	18	22	26	30
	3	7	11	15	19	23	27	31
	4	8	12	16	20	24	28	32

(b)								
WVC	4C	3D	2D	1C	1B	2A	3A	4B
Az Bins that	1	4	9	14	17	20	25	30
go into WVC	2	5	10	15	18	21	26	31
	3	6	11	16	19	22	27	32
		7	12			23	28	
		8	13			24	29	

The data stream is delayed by units of 1/32 sec to get the next sigma-0 value and each value is designated to respective WVC using the table. After 32 delays, data from the next scan starts. Data from 8 scans are placed into the same WVC after which the data are assigned to the next WVC along track. Table 3.2 shows location of each azimuth bin from 24 subsequent scans. It may be noted that after every 8 scans the measurement falls into next WVC.

The algorithm thus uses the aircraft altitude and velocity, beam incidence angle, WVC size and scan rate as inputs and calculates the locations of each sigma-0 binned measurement into respective WVC in the grid.

Table 3. 2 Location of sigma-0 measurements from multiple scans.

Az bin Scan no	1	2	3	4	5	6	7	8	25	26	27	28	29	30	31	32
1	1c	1c													1b	1b
2	1c	1c													1b	1b
3	1c	1c	1c												1b	1b
4	1c	1c	1c	1d									1a	1b	1b	1b
5	1c	1c	1c	1d									1a	1b	1b	1b
6	1c	1c	1c	1d	1d							1a	1a	1b	1b	1b
7	1c	1c	1c	1d	1d							1a	1a	1b	1b	1b
8	1c	1c	1c	1d	1d							1a	1a	1b	1b	1b
9	2c	2c	1c	1c	1d						1a	1a	1a	1b	2b	2b
10	2c	2c	2c	1d	1d	1d					1a	1a	1a	2b	2b	2b
11	2c	2c	2c	1d	1d	1d					1a	1a	1a	2b	2b	2b
12	2c	2c	2c	2d	1d	1d	1d			1a	1a	1a	2a	2b	2b	2b
13	2c	2c	2c	2d	1d	1d	1d			1a	1a	1a	2a	2b	2b	2b
14	2c	2c	2c	2d	1d	1d	1d	1d	1a	1a	1a	1a	2a	2b	2b	2b
15	2c	2c	2c	2d	2d	1d	1d	1d	1a	1a	1a	2a	2a	2b	2b	2b
16	2c	2c	2c	2d	2d	1d	1d	1d	1a	1a	1a	2a	2a	2b	2b	2b
17	3c	2c	2c	2d	2d	2d	1d	1d	1a	1a	2a	2a	2a	2b	2b	3b
18	3c	3c	2c	2d	2d	2d	1d	1d	1a	1a	2a	2a	2a	2b	3b	3b
19	3c	3c	3c	2d	2d	2d	1d	1d	1a	1a	2a	2a	2a	3b	3b	3b
20	3c	3c	3c	3d	2d	2d	2d	1d	1a	2a	2a	2a	3a	3b	3b	3b
21	3c	3c	3c	3d	2d	2d	2d	1d	1a	2a	2a	2a	3a	3b	3b	3b
22	3c	3c	3c	3d	2d	2d	2d	1d	1a	2a	2a	2a	3a	3b	3b	3b
23	3c	3c	3c	3d	3d	2d	2d	2d	2a	2a	2a	3a	3a	3b	3b	3b
24	3c	3c	3c	3d	3d	2d	2d	2d	2a	2a	2a	3a	3a	3b	3b	3b

With the outer (40 deg incidence) beam, the scan geometry gives typically 3 azimuth binned sigma-0 measurement for each polarization in the two WVC's closest to the sub-track (WVC's b & c in Fig. 3.1). For the same WVC's, the inner beam (30 deg Inc) gives 4 measurements for each polarization per scan; and in the case of outer WVC's (a & d in Fig. 3.1), there are 5 azimuth binned measurement for each polarization with the outer beam and 4 measurements for the inner beam, per scan. At a scan rate of 60 rpm and an aircraft velocity of 125 m/s there are typically 8 scans inside a 1 Km WVC for each forward and aft look. For each look, this means that there are up to 24 and 32 measurements with the outer and inner beams, respectively for the inner WVC's separately; and for the outer WVC's, there are up to 40 and 32 measurements with the outer and inner beams, respectively. Similar measurements (which have same incidence, look, azimuth bin and polarization) are averaged to speed the wind retrieval computation time.

Table 3.3 Number of independent azimuth binned measurements.

Number azimuth measurements		Inner WVC	Outer WVC
Fwd look	Inner beam (30 deg)	4x8 H + 3x8 V = 56	3x8 H + 3x8 V = 48
	Outer beam (40 deg)	4x8 H + 4x8 V = 64	5x8 H + 5x8 V = 80
Aft look	Inner beam (30 deg)	3x8 H + 3x8 V = 48	3x8 H + 3x8 V = 48
	Outer beam (40 deg)	4x8 H + 3x8 V = 56	5x8 H + 5x8 V = 80

3.3 Effects of attitude variations

As the aircraft flies through the hurricane, normally there will be attitude variations (roll and pitch) because of turbulence or other flight dynamics factors. Any change in the aircraft attitude, directly affects the radar scanning pattern on the surface by misaligning the antenna spin axis, which results in elliptical scan patterns on the surface and variable incidence angle over a revolution [18]. For typical small angles of attitude variation, the polarization rotation effect is not significant, hence, it is neglected. The three aircraft attitude parameters are roll, pitch & yaw, which are rotations about the aircraft inertial coordinate system axes. Pitch is a measure of the degree to which an aircraft's nose tilts up or down, roll is the rotation of the wings about an axis aligned with the flight direction, and yaw is the angle between a vehicle's heading and its direction of travel or track. Yaw angle does not change the conical scan geometry as it is rotation within the horizontal plane; but it does affect the collocations within a WVC.

To study the effect of attitude on the IWRAP scan geometry, a typical value of ± 2 deg changes in roll and pitch was applied to the scan geometry and the effect on the ground pattern was observed. The results of the study are presented in Fig. 3.4 through 3.9.

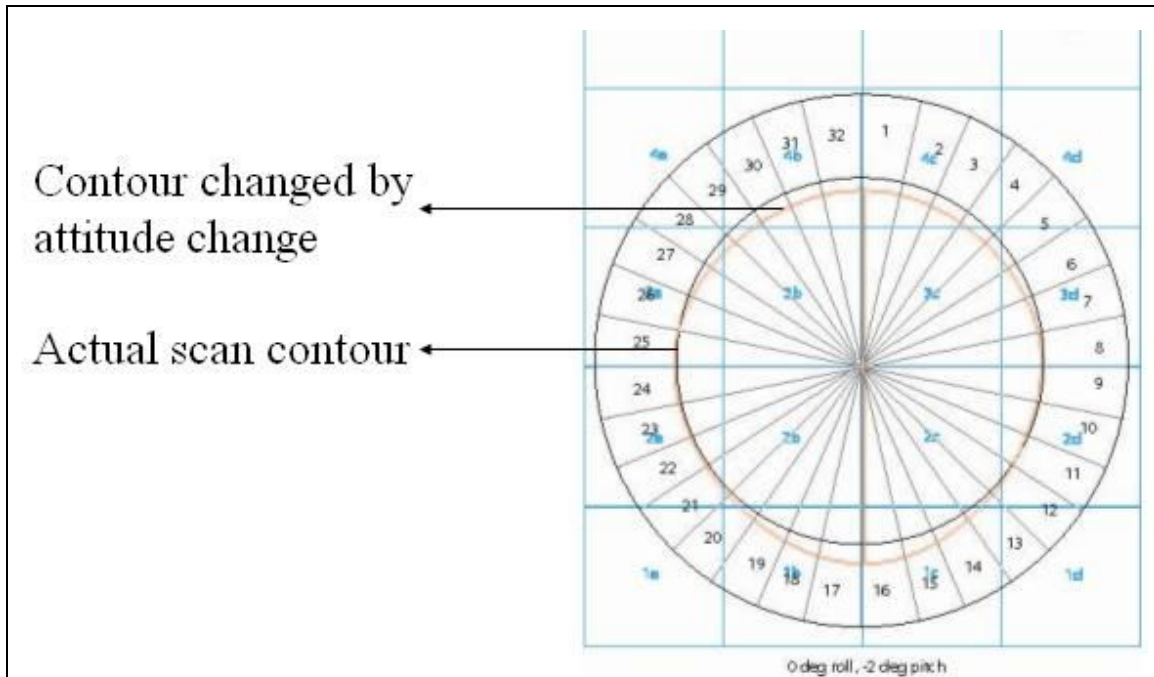


Figure 3.4 Effect of 0 deg roll -2 deg pitch variation on scan contour.

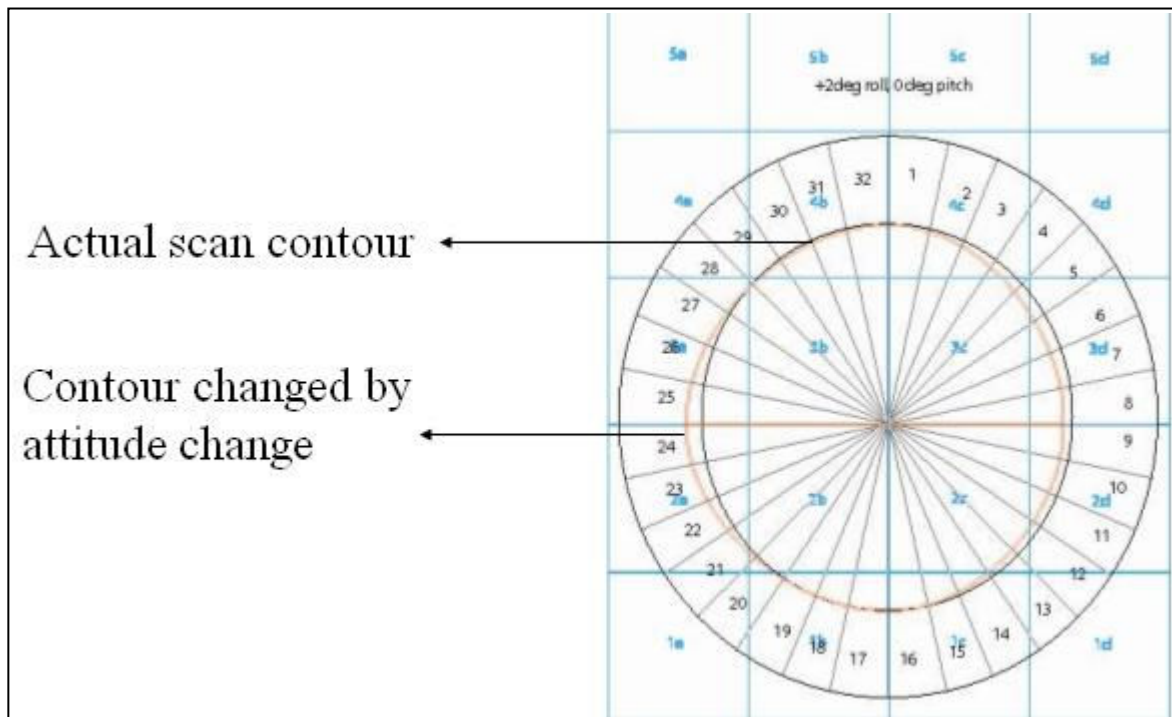


Figure 3.5 Effect of +2 deg roll 0 deg pitch variation on scan contour.

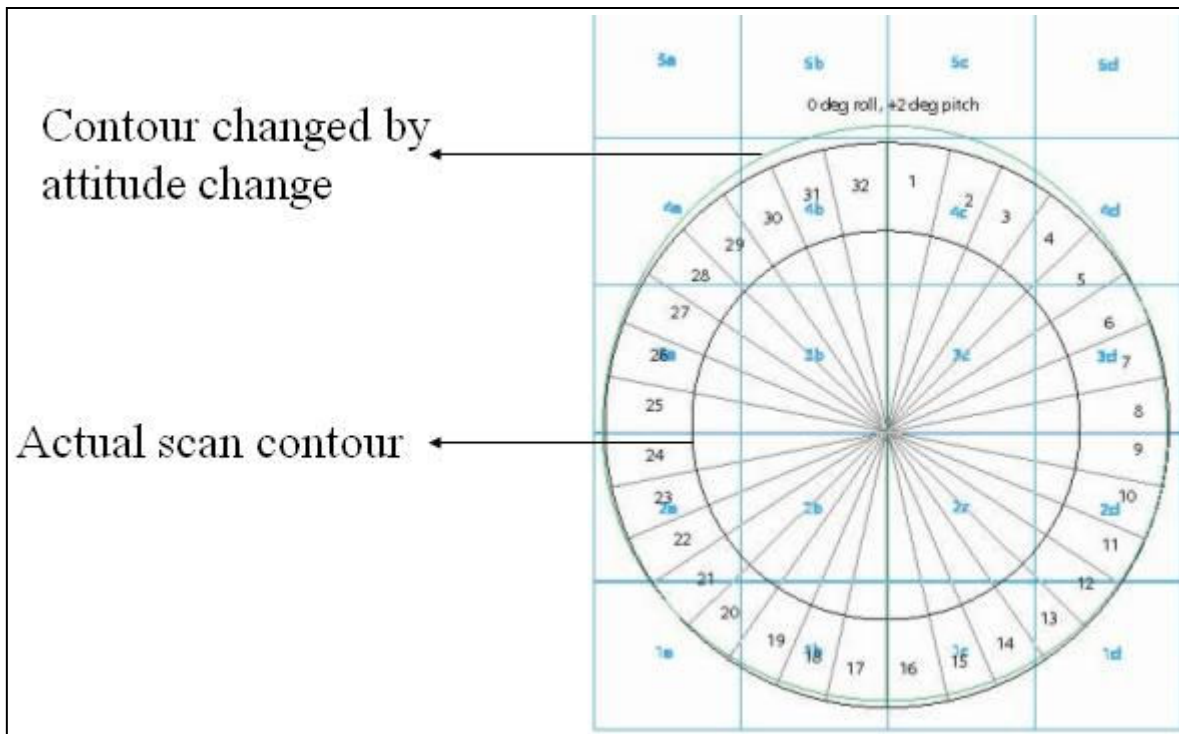


Figure 3.6 Effect of 0 deg roll +2 deg pitch variation on scan contour.

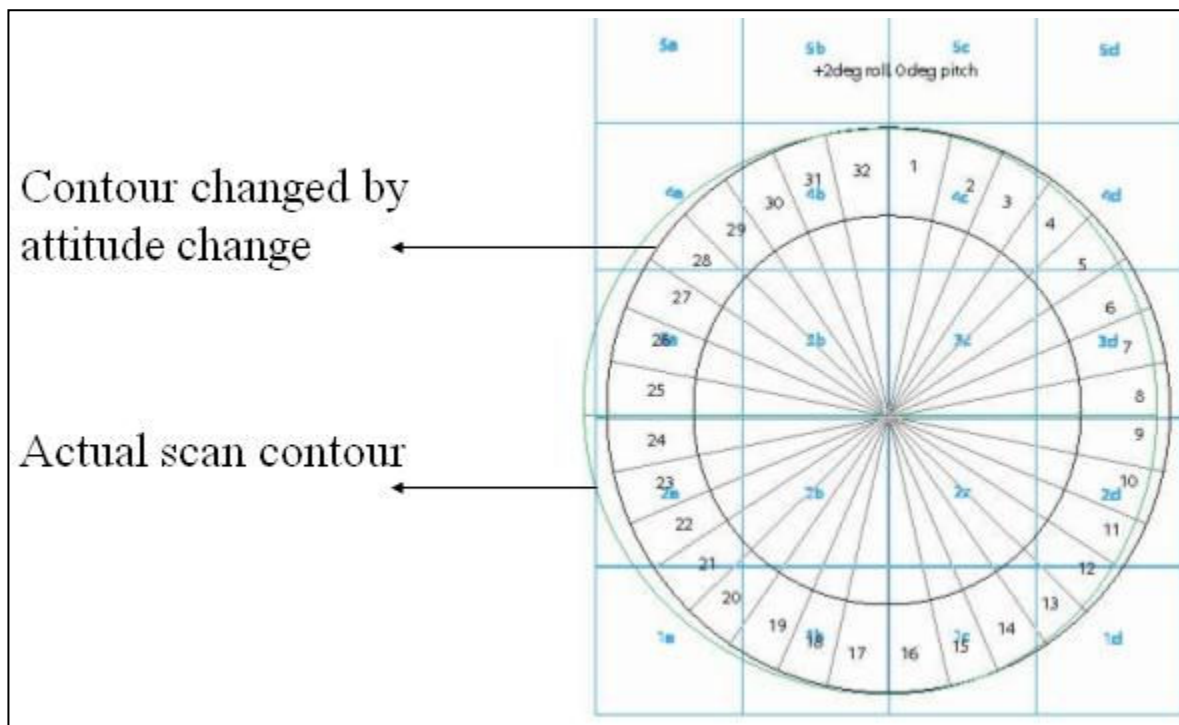


Figure 3.7 Effect of +2 deg roll 0 deg pitch variation on scan contour.

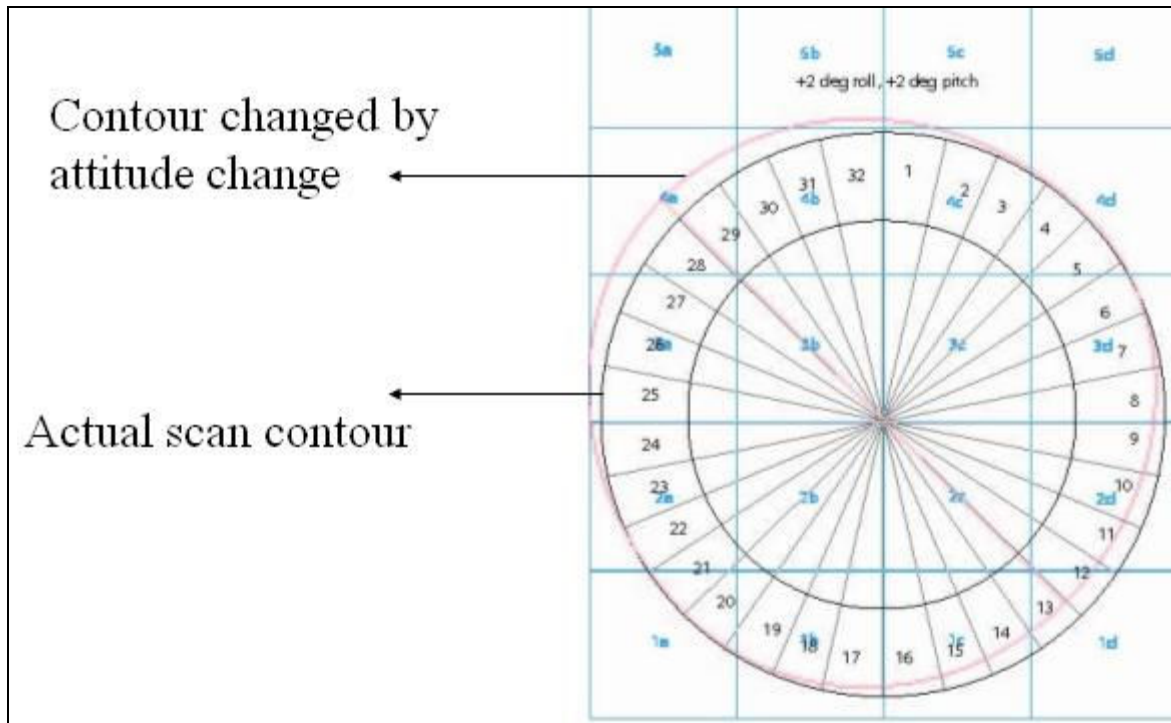


Figure 3.8 Effect of +2 deg roll +2 deg pitch variation on scan contour.

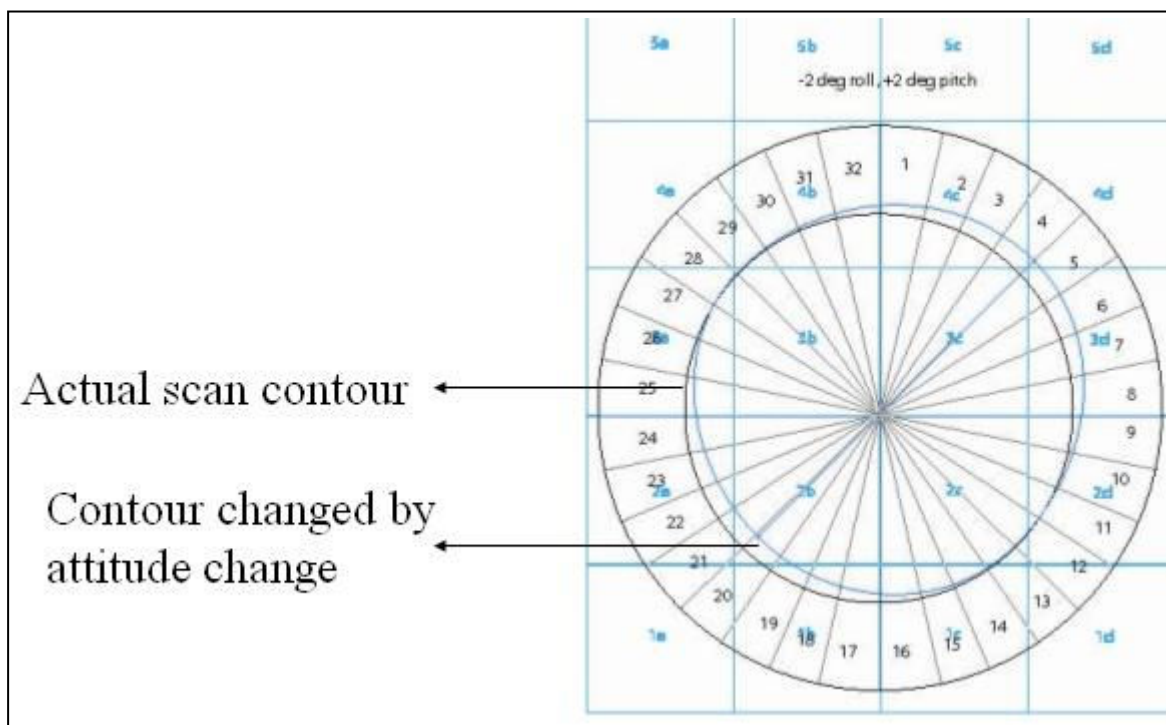


Figure 3.9 Effect of -2 deg roll -2 deg pitch variation on scan contour.

From the results of the analysis, it can be seen even with the case of 2 deg change in both pitch and roll, the effect on geo-location of the footprint is not significant enough for the WVC grouping of the measurement to be changed. Hence it was concluded that there was no adaptation required to the scan geometry to account for the time varying attitude of the aircraft.

The collocation algorithm is easily adapted to other conical scanning configurations and the new delays to accommodate changes in aircraft altitude and velocity and radar incidence angle can be provided in tabular form, which is used as an input to the algorithm.

CHAPTER 4: DESIGN OF WIND RETRIEVAL ALGORITHM

4.1 Background of Wind Vector Retrieval

The backscattered sigma-0 data must be interpreted to retrieve wind speed and direction measurements. Inversion of radar backscatter measurements relies on empirically derived relationship between the sigma-0 and ocean surface wind vector known as geophysical model function (GMF). According to Fernandez et al. [17], “*Physically based theoretical models are not used due to insufficient knowledge of the complex relationship between the sea surface roughness and environmental (wind forcing) conditions, and electromagnetic scattering mechanisms from rough ocean surfaces*”. Conventional satellite GMF’s have well established their ability to measure normal wind speeds over the oceans. However, when it comes to measuring hurricane force wind speeds, “*the conventional GMF’s have been shown to over predict the NRCS values for high wind speeds, and thus wind speeds derived using these GMF’s significantly underestimate actual surface wind speeds for tropical cyclones*”. Scatterometer wind retrievals have been found to be anomalously low in various studies that were performed. Consequently, special ocean surface sigma-0 geophysical model functions for high wind speeds using satellite based scatterometer sigma-0 measurements [19] were developed.

In this thesis, the special GMF used herein is tailored to measure high wind speeds by using aircraft measurements in tropical cyclones, which is explained in detail, in the following sections.

4.2 Geophysical Model Function

A geophysical model function (GMF) provides the relationship between the radar observable (σ_0) and the surface wind vector (speed and direction). The GMF depends on the radar measurement geometry- incidence angle, polarization and azimuth look direction. In all, the GMF is a function of:

- Wind Speed
- Relative Wind Direction (angle between the surface wind direction and the σ_0 measurement azimuth look direction)
- Incidence Angle (angle between the normal to surface and antenna line of sight between radar and the surface)
- Beam Polarization - horizontal or vertical

Knowing four of the five inputs allows one to use root finding algorithms to determine the remaining parameter. The C-band & Ku-band high wind speed GMF's used in this wind retrieval algorithm were developed from experimental airborne scatterometer data obtained over 10 years of NOAA-Hurricane Research Division (HRD) & University of Massachusetts (UMASS) flights through hurricanes [15, 16].

“These GMF's are developed by adding terms to a conventional power law, where the σ_0 is proportional to the neutral stability wind speed measured at a height 10 m above the ocean surface U_{10N} raised to a power. These terms permit a slow roll-off in the power law wind exponent and allows the saturation wind speed ($U_{10N_{sat}}$) to be determined. $U_{10N_{sat}}$ is defined as the wind speed where the mean σ_0 , A_0 reaches its maximum value, i.e.:

$$\frac{\partial A_0}{\partial U_{10N}} \Big|_{U_{10N} = U_{10N \text{ sat}}} = 0 \quad (4.1)$$

To model the departure from a power law, it is enough to add one more term at C-band, resulting in a parabolic fitting in a space where both wind speed and the A_0 are logarithmic. At Ku-band the rapid decrease in the A_0 at high wind speeds requires a higher order polynomial, and so a cubic fitting in log-log space has been used. The functional form of C-band high wind speed GMF A_0 is thus given by:

$$A_{0 \text{ dB}}(U_{10N}) = 10 [\beta + \gamma_1 \log_{10}(U_{10N}) + \gamma_2 [\log_{10}(U_{10N})]^2] \quad (4.2)$$

where, A_0 is in dB.

At Ku band, the functional form of high wind speeds GMF is given by:

$$A_{0 \text{ dB}}(U_{10N}) = 10 [\beta + \gamma_1 \log_{10}(U_{10N}) + \gamma_2 [\log_{10}(U_{10N})]^2 + \gamma_3 [\log_{10}(U_{10N})]^3] \quad (4.3)$$

where, A_0 is in dB

$\beta, \gamma_1, \gamma_2$ and γ_3 are coefficients, determined using least square regression. Table 4.1 lists the values of the coefficients.”

Table 4.1 Values of coefficients β , γ_1 , and γ_3 .

Band	Pol.	Inc (deg)	β	γ_1	γ_2	γ_3
C	VV	30	-3.9718	4.1794	-1.208	
C	HH	40	-5.081	4.784	-1.266	
C	VV	30	-4.7326	4.61436	-1.34374	
C	HH	40	-5.47971	4.722471	-1.1822	
Ku	VV	30	49.842	-97.53	62.7112	-13.341
Ku	HH	40	28.20978	-58.8867	39.34656	-8.62156
Ku	VV	30	12.60833	-27.1743	18.56383	-4.13983
Ku	HH	40	16.49414	-36.2399	24.603	-5.41414

Table 4.2 lists $U_{10N_{sat}}$ values for C and Ku band for each incidence angle.

Table 4. 2 Saturation wind speed values.

Band	Pol.	Inc (deg)	$U_{10N_{sat}}$
C	VV	30	53.7
C	HH	40	60.5
C	VV	30	52.64
C	HH	40	65.0
Ku	VV	30	50.76
Ku	HH	40	52.12
Ku	VV	30	51.12
Ku	HH	40	58.13

“The high wind speed GMF must also include the wind directional anisotropy in the sigma-0. The functional form for this is modeled by the expression given below:

$$\begin{aligned}\sigma^0(\theta, U_{10N}, \chi) = & A_0(\theta, U_{10N}) [1 \\ & + a_1(\theta, U_{10N}) \cos(\chi_{rel}) \\ & + a_2(\theta, U_{10N}) \cos(2\chi_{rel})]\end{aligned}\quad (4.4)$$

where, $\chi_{rel} = \chi_{up} - \chi$, is the relative wind direction

$\sigma^0 = NRCS$ and $\theta = inc$ angle

$$\begin{aligned}a_1(\theta, U_{10N}) = & c_0(\theta, U_{10N}) + c_1(\theta, U_{10N}) \cdot U_{10N} \\ & + c_2(\theta, U_{10N}) \cdot U_{10N}^2\end{aligned}\quad (4.5)$$

$$\begin{aligned}a_2(\theta, U_{10N}) = & d_0(\theta, U_{10N}) \\ & + d_1(\theta, U_{10N}) \cdot U_{10N} \\ & + d_2(\theta, U_{10N}) \cdot \tanh\left(\frac{U_{10N}}{d_3(\theta)}\right) \cdot U_{10N}\end{aligned}\quad (4.6)$$

The first harmonic is thus modeled by a second order polynomial and the second harmonic by a linear relationship plus a hyperbolic tangent to capture the saturation at high wind speeds. Setting the d_3 values to those derived by Donnelly et al. [15], the other coefficients can be derived by linear regression. The values for the coefficients are given in Table 4.3 and 4.4.”

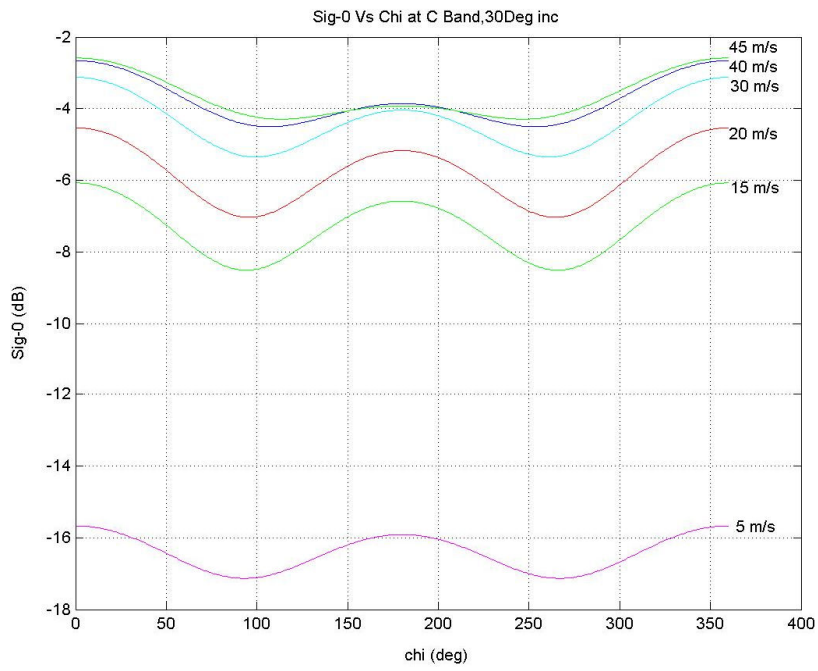
Table 4.3 Coefficients for eq 4.5

Band	Pol.	Inc (deg)	C ₀	C ₁	C ₂
C	VV	30	0.00984	0.004543	-2.3E-05
C	HH	40	-0.1757	0.01515	-0.00015
C	VV	30	0.10602	0.001004	4.76E-05
C	HH	40	0.133714	0.001577	-3.2E-06
Ku	VV	30	0.136596	-0.00684	0.000124
Ku	HH	40	0.085391	-0.00323	6.19E-05
Ku	VV	30	0.268817	-0.01206	0.000164
Ku	HH	40	0.237616	-0.0105	0.000144

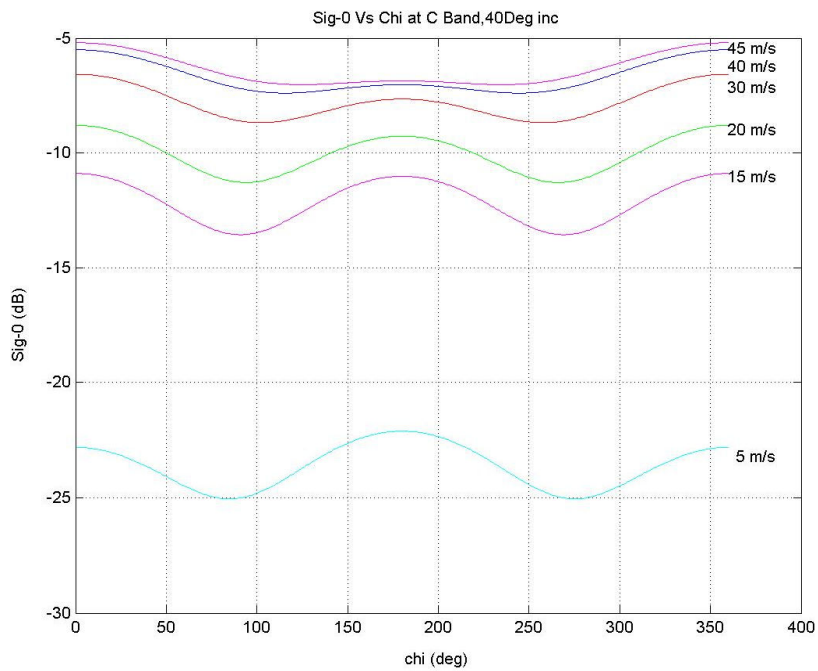
Table 4. 4 Coefficients for eq 4.6

Band	Pol.	Inc (deg)	d ₀	d ₁	d ₂	d ₃
C	VV	30	0.039592	0.02763	-0.02834	28
C	HH	40	0.1972	0.02561	-0.02837	18
C	VV	30	0.20966	-0.0068	0.003126	32
C	HH	40	0.3244	-0.0105	0.005018	17.71429
Ku	VV	30	-0.844	0.15906	-0.14398	22.4
Ku	HH	40	-0.15591	0.481467	-0.47636	11.88889
Ku	VV	30	-0.52395	0.1209	-0.10992	22.5
Ku	HH	40	-0.06735	0.354071	-0.3505	12.14286

To illustrate the effect of wind speed and direction on the σ_0 values generated by the GMF, the responses are presented in Fig. 4.1 and 4.2 for C- and Ku- band respectively. It is worth noting that the relative wind anisotropy dampens at higher wind speeds.

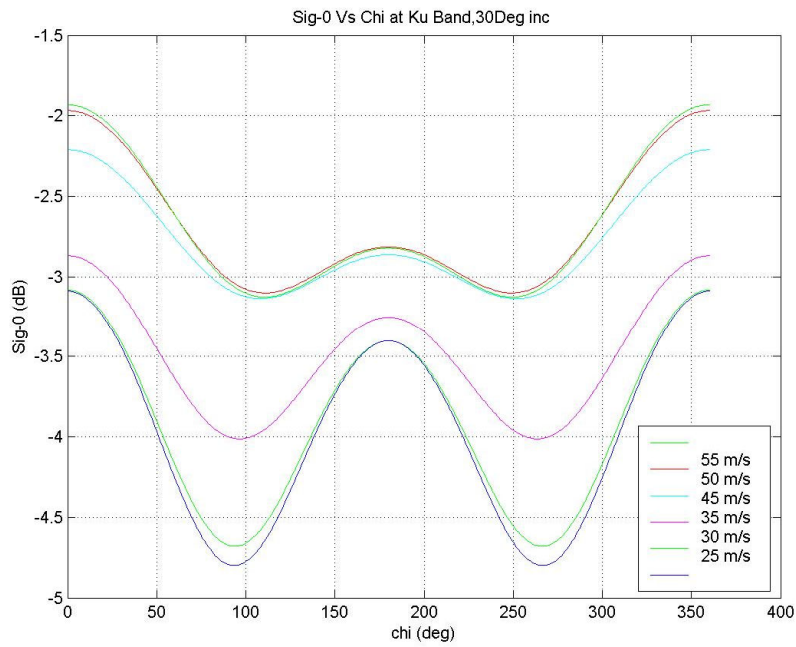


a. 30 deg incidence.

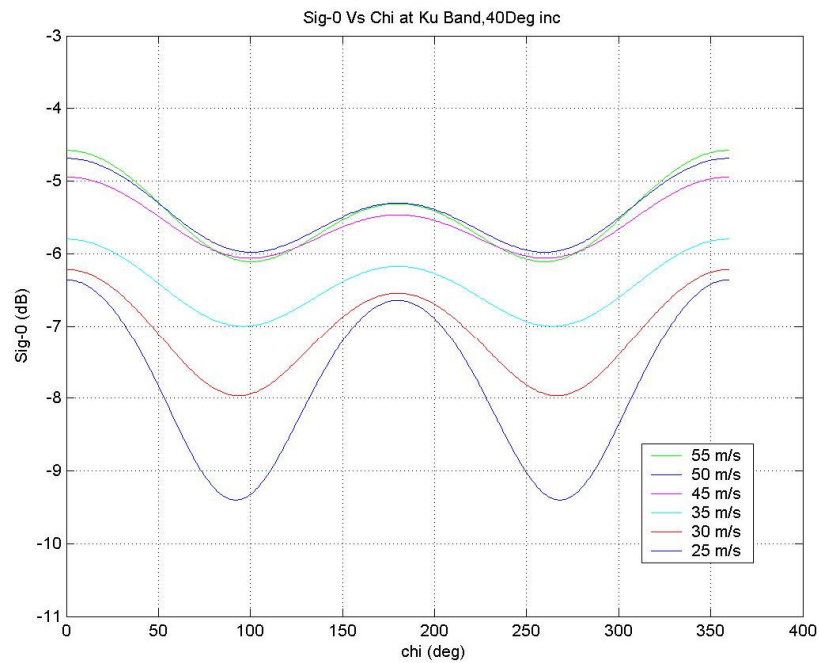


b. 40 deg incidence.

Figure 4.1 Response of GMF at various wind speeds for C band.



a. 30 deg incidence.



b. 40 deg incidence.

Figure 4.2 Response of GMF at various wind speeds for Ku band.

4.3 Design and Testing of Wind Retrieval Algorithm

4.3.1 Maximum Likelihood Estimator

A method of retrieving wind vector speed and direction from the measured sigma-0 values is using the process of maximum likelihood estimation, as applied to statistical parameter estimation [19]. This method maximizes the joint probability density of a set of residuals (sigma-0 measurements minus GMF)². This is equivalent to finding the most likely set of the model parameters (wind speed and direction) which produced the observed sigma-0's. The Gaussian probability density P_i for a given sigma-0 measurement S_i compared to a corresponding GMF value F_i is given by:

$$P_i = (2\text{Var}(S_i))^{-1} \exp\left\{-\frac{(S_i - F_i)^2}{2\text{Var}(S_i)}\right\} \quad (4.7)$$

where, the variance ($\text{Var}(S_i)$) of the sigma-0 measurement is estimated from the instrument parameters and the backscattered signal to noise ratio. The likelihood function is the joint probability density, P , defined as the product of the P_i over the n measurements in the wind vector cell.

To maximize the joint probability density of a set of residuals, the difference of sigma-0 measurements and GMF, the following equation is used:

$$\text{cost function} = \sum_{i=1}^n \left(\frac{(\sigma_{i(\text{measured})}^0 - \sigma_{i(\text{modelled})}^0)^2}{\delta^2} \right) \quad (4.8)$$

where,

δ = variance of the sigma-0 measurement

n =no of independent measurements

Because of the harmonic nature of the GMF, multiple wind solutions are produced, and the number of solutions ranges from two to four depending upon the relative wind direction χ , at which the measurements were made. The cost function is calculated for a combination of possible range of wind speeds and directions in steps. This creates a two dimensional surface for every measured value of sigma-0 in a WVC. These surfaces are combined to form one surface for every WVC, called the cost surface, with each point on the surface representing the cost function for a particular combination of wind speed and direction, calculated by Eq 4.8. Every local minimum on this surface represents a potential solution for wind speed and direction.

Figure 4.3 shows a best solution at the “tight” intersection of four curves from different beams of a scatterometer. Because the wind speed versus wind direction solution curves shift laterally with changes in the value of χ , this causes the number of points (solutions) at which the curves intersect to vary. These multiple solutions, called aliases or ambiguities, are nearly equal in wind speed but vary in wind direction over the full range of 360°. For the case of two aliases, they generally differ by about 180°. The probability that a given solution is the correct wind can be estimated by the relative value of its likelihood function; therefore, the retrieved wind vectors are ranked according to this criterion (i.e., according to the depth of the local minima).

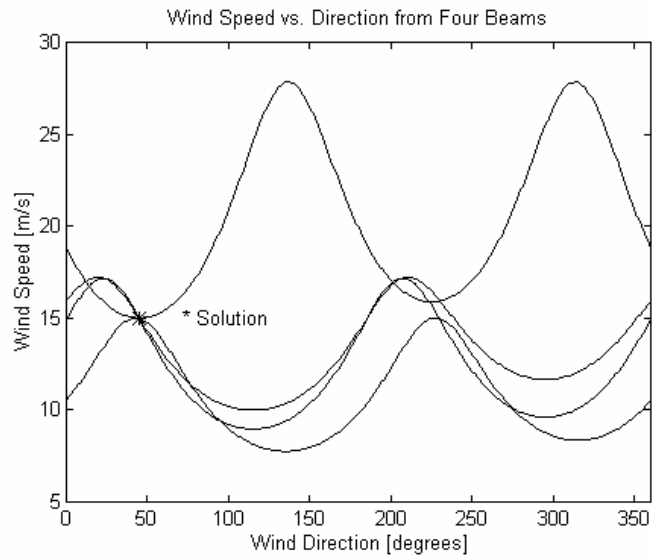


Figure 4.3 Best wind vector solution occurs at “tightest” intersection of four curves.

The last step in the wind vector retrieval algorithm is the refinement in the retrieved wind direction (selection of the best alias) known as wind-direction alias-removal. The most common approach uses the wind solution rankings and a median filter technique to select a single wind direction, and the accuracy of this procedure is estimated to be better than 90% for satellite retrievals. The same approach of solution rankings is applied in this retrieval algorithm; but not median filtering.

For our algorithm, once the ‘cost surface’ is calculated, a separate searching algorithm searches for the local minima on the surface. A sliding window search scheme is applied to search the minima on the surface. An $(n \times n)$ window (where n is selectable) is moved across the surface in steps of one pixel and for every step, the algorithm checks if the center value in the box is the lowest value in the window; if so it is declared as a local minima and the MLE

value(cost function) for that pixel is recorded. Once the algorithm scans the entire surface and finds all the local minima, it picks the lowest four values and discards the remaining minima. The four values are then ranked, with the lowest value being given the highest rank. Each set of wind speed and direction values for each of the four minima is a possible solution. The highest ranked minimum has the maximum probability of being the correct solution; but the presence of noise can result in the correct solution being lower ranked. The algorithm tags the value with highest rank as the most probable solution for the WVC, also considering the other solutions.

One of the challenges in designing this wind retrieval algorithm is to achieve fast processing speed in order to make real-time wind retrieval possible. To achieve this, several adaptations were needed; and they are explained below. Calculating the cost surface for the full wind direction range of 360 degrees is computationally demanding because, for every wind direction value, the MLE value needs to be calculated using Eq 4.8.

To speed up the computation time, two approximations are made. First, an estimate of wind speed is made by neglecting the relative wind direction and comparing the average of the measured σ_0 's to an isotropic σ_0 (averaged over all wind directions) versus wind speed (Fig. 4.4). This estimated wind speed may be in error by a few m/s because we have neglected the true relative wind directions of each σ_0 ; but as a result, the wind speed search space can be reduced to a small range around the first guess value. Experimentally, it was verified that a window size of ± 4 m/s about the estimated value was sufficient to capture all possible solutions.

Second, instead of calculating a cost surface for full 360 deg of possible relative wind direction, the cost surface can be reduced by restricting the range of wind directions. This is accomplished using the flight level wind direction, which is measured directly with inertial

navigation instrumentation on board the aircraft. Restricting the search space to ± 60 deg around the flight-level wind direction provides a sufficient range to capture all likely solutions; so we select the highest ranked alias within this reduced surface. This has the added advantage of greatly reducing the area of the cost surface and hence the computation time. Reduced surface area means lesser searching time to the local minima searching algorithm, as the algorithm has to scan though the entire surface searching for minima. The difference may be noted by comparing Figs 4.5 and 4.6.

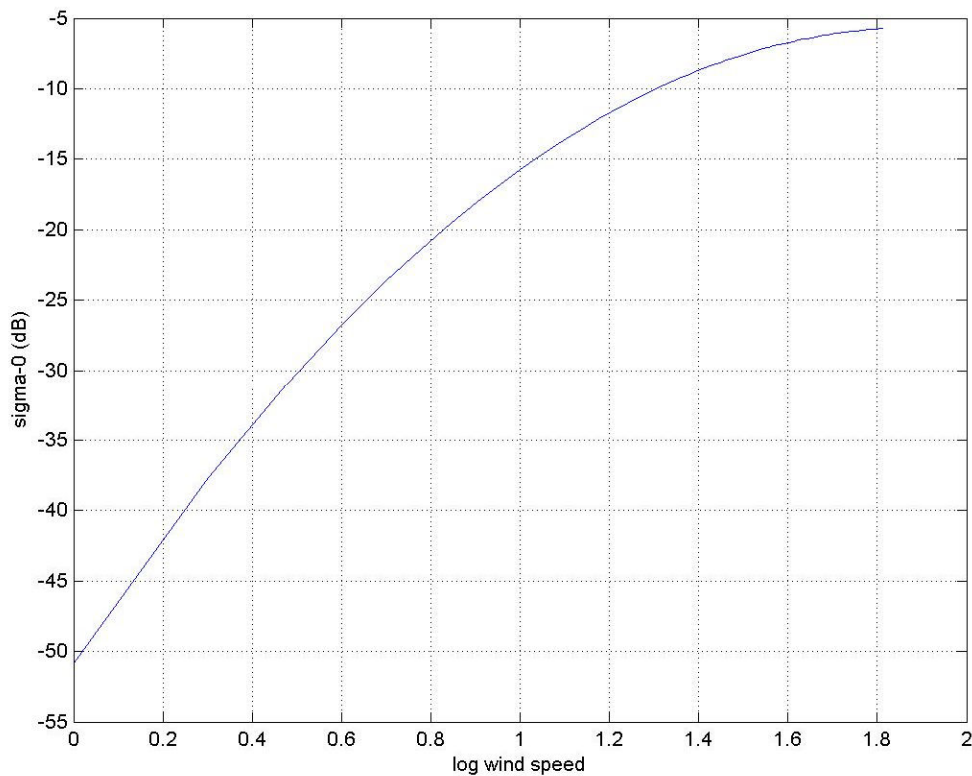


Figure 4.4 Isotropic Sigma-0 at C band V-pol for 40 deg incidence.

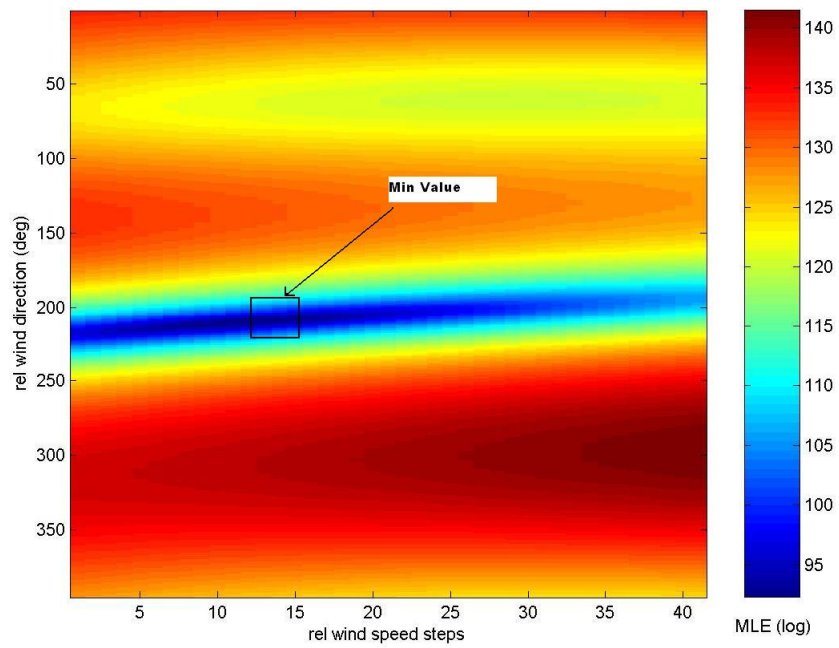


Figure 4.5 Cost Surface for wind direction range of 360 deg and wind speed ± 4 m/s.

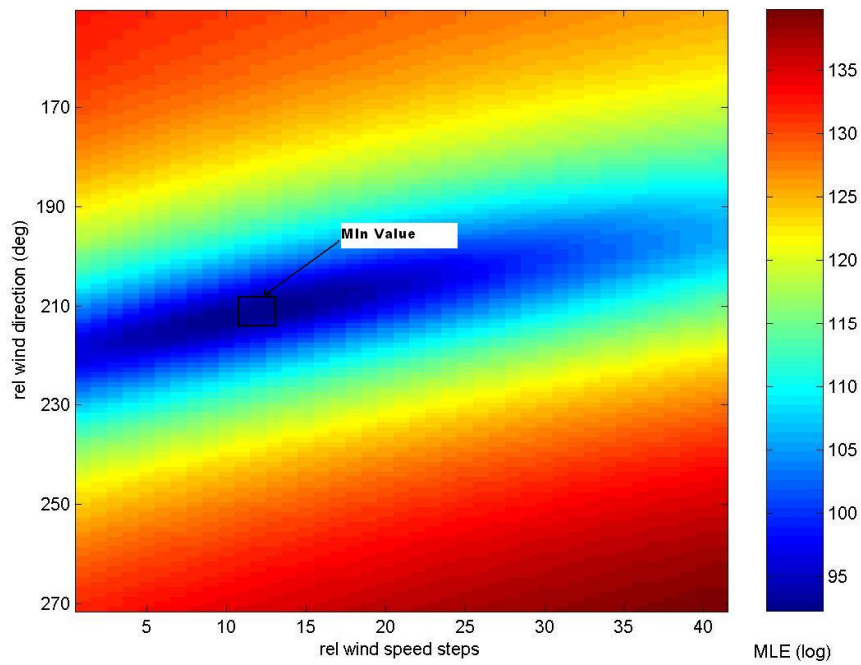


Figure 4.6 Cost surface: calculated at ± 60 deg of flight level wind direction and wind speed ± 4 m/s.

Figure 4.6 shows the cost surface calculated for the reduced range of wind speeds $\pm 4\text{m/s}$ about the estimated value, in steps of 0.2 m/s , $0\text{-}360$ degrees in steps of 1 deg . This means that there are $360 \times 40 = 14400$ discrete points on the surface for which MLE value have to be calculated. Figure 4.7 on the other hand, shows the case where the wind direction is restricted to ± 60 degrees around the flight level wind-direction. There are 120 , 1-deg steps in one dimension and 40 steps of 0.2 m/s in the other dimension. In this case, there are $120 \times 40 = 4800$ discrete points, as opposed to 14400 in the previous case. This means a reduction in processing time by a factor of three.

4.3.2 Compass Simulation

A simple, but reliable, method to perform preliminary testing of the retrieval algorithm is to use the conical scanning measurement geometry to sample a constant wind-field and then calculate the corresponding σ_0 using the GMF, for various combinations of wind speeds and directions. Afterwards, the simulated σ_0 's are used to retrieve the wind speed and direction with the retrieval algorithm. The process is repeated as a Monte Carlo simulation by adding Gaussian random noise to the generated σ_0 values. Figure 4.8 illustrates a few test cases in the compass simulation. The retrieved values are compared statistically with the true values for the quality of retrieval. This method is called compass testing, and it provides a means for evaluating the retrieval algorithm for simple noisy cases. The results for compass testing are presented below.

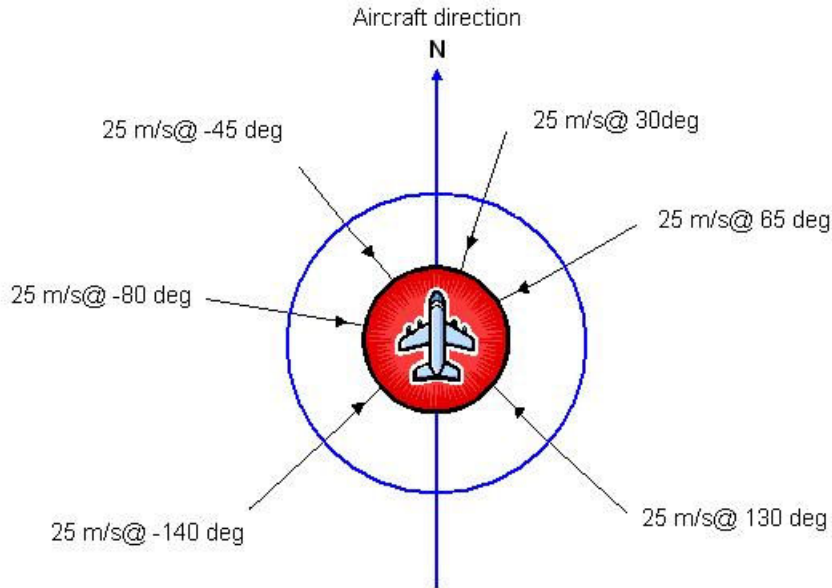
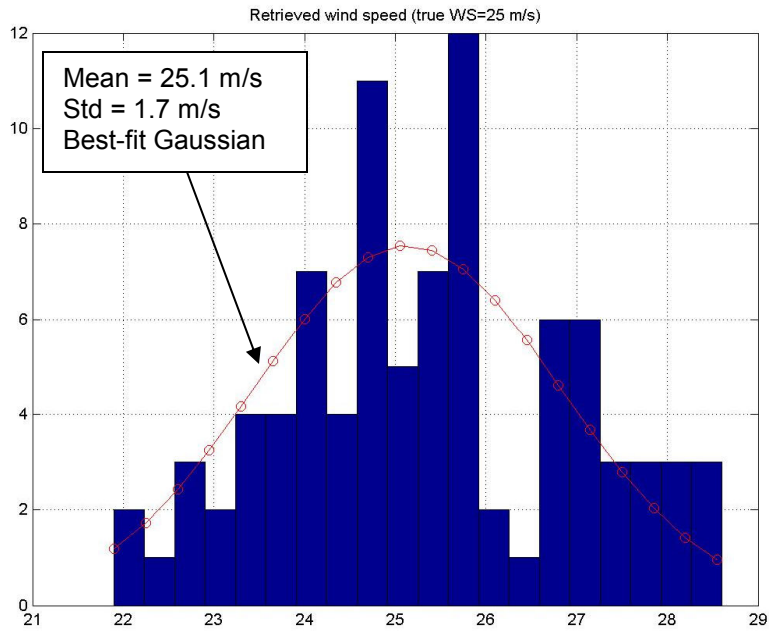


Figure 4. 7 Typical compass testing cases.

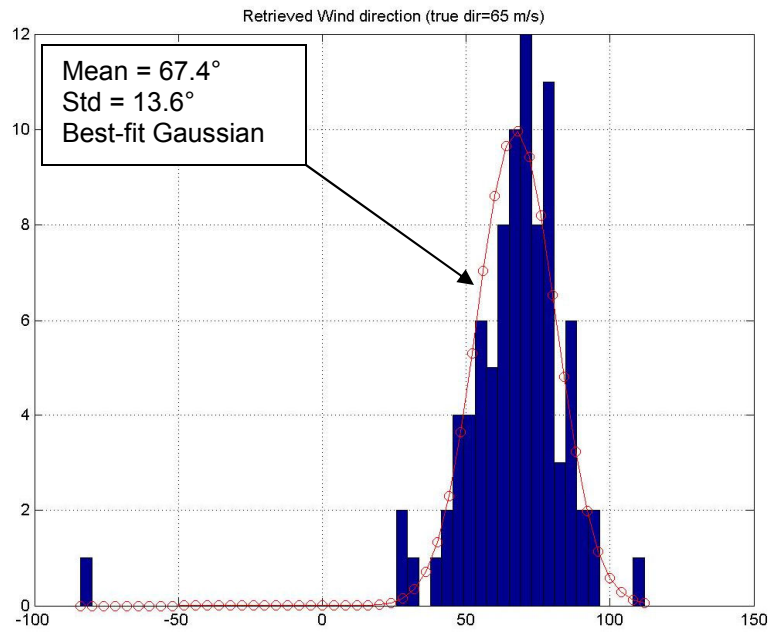
When the simulation is performed by without adding any noise, the difference between the true value and the retrieved value is near zero, as expected; whereas, with the addition of Gaussian random noise, the retrieved values are Gaussian distributed about the true value. This can be observed in the histogram of one of the simulation results, shown in Fig. 4.8. Panel (a) shows the histogram of the retrieved wind direction values for compass test case, where the true wind speed was 25 m/s and the true wind direction, 65 deg. The histogram represents a hundred independent retrieved values, each one with a different sample of zero mean Gaussian random noise added. The noise that was added, was a Gaussian random variable with zero mean and a standard deviation equal to 30 % of the true value. The plotted line over the histogram is the best Gaussian curve fit. It is calculated by fitting a curve to the histogram values, such that the squared error between the true area and the area covered by the curve is minimum. The mean and

the standard deviation of the retrieved values after performing the Gaussian fit was found to be 25.1 m/s and 1.7 m/s respectively.

Similarly Panel (b) shows the histogram of the retrieved wind direction values. In this case, the mean and the standard deviation of the retrieved values after performing the Gaussian fit was found to be 67.4 deg and 13.7 deg respectively, compared to the true value of 65 deg. This demonstrates that the retrieval algorithm performed well for the simple noisy test case. These results were as expected, and they give the confidence that the retrieval algorithm works properly.



a. Wind speed results for original wind speed of 25m.



b. Wind direction results for Original wind direction of 65 deg.

Figure 4 8 Compass testing: difference between retrieved and true wind speed and direction.

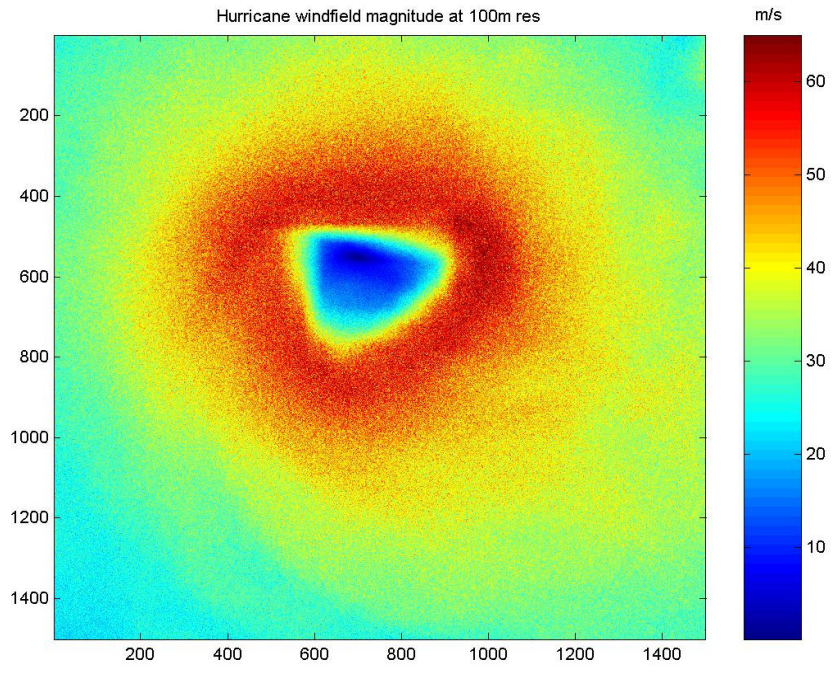
CHAPTER 5: EXPERIMENTAL VALIDATION

5.1 Simulation of aircraft over-flight

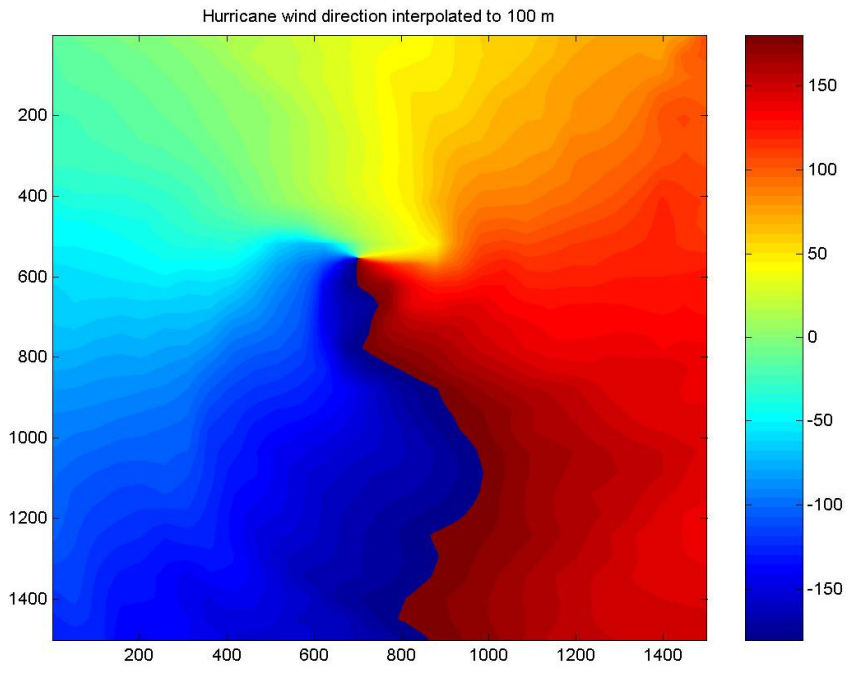
5.1.1 Hurricane wind field simulation

The wind retrieval algorithm needed to be tested for its performance in a real-time scenario. Only in a real-time test, would the performance of the retrieval algorithm under the constrain of time, be observable. In the absence of actual streaming sigma-0 data from the IWRAP instrument, this data was required to be simulated.

In order to simulate hurricane wind vector retrieval, a realistic hurricane wind field was created with using numerical weather model calculation for hurricane Floyd, acquired from NOAA – Hurricane Research Division (HRD). These data were interpolated to obtain a wind field resolution of 100 m x 100 m; and to overcome the ‘smoothness’ generated by interpolation, random noise was added to the wind field. First the interpolated modeled wind vector field was broken into orthogonal North/South (‘U’) and East/West (‘V’) components. Next, independent noise was added to each component as Gaussian random additive noise with zero mean and a standard deviation equal to 10 % of mean value of the simulated wind-field component. Finally, the components were combined to yield wind speed and direction, which simulates the small-scale wind turbulence that occurs in nature (but was missing from the smoothed model results). This makes the simulation closer to real hurricane wind field observations; and the wind field thus generated is shown in Fig. 5.1 a & b.



a. Wind speed.



b. Wind direction.

Figure 5.1 Simulated hurricane wind field with noise added.

5.1.2 Simulated radar measurements

To simulate a real-time scatterometer measurement scenario, there had to be simulated geometry (conical scanning) and sigma-0 measurements to yield a time-series multiplexed output along the scan. These sigma-0's were used to perform real-time wind vector retrieval. The conical scanning simulation was performed by using the geometry for the IWRAP instrument specifications and the aircraft flight altitude to calculate the footprint center locations accordingly. Figure 5.2 shows these locations for the outer (40 deg) beam as the antenna scans from an aircraft altitude of 2.2 Km using a pixel size of 100 m x 100 m. It may be noted that pattern generated in Fig. 5.2 is spiral, which is as a result of the instrument conical scanning, and the aircraft's motion.

First, the sigma-0 generator program calculates the geo-locations of these footprints, and then interpolates the corresponding wind speed and direction from the gridded simulated hurricane wind field (discussed earlier) and calculates the relative wind direction using the corresponding radar azimuth. Once the wind speed and relative wind direction for the pixels are known, the program uses the GMF to calculate sigma-0 values for both polarizations and frequency bands, for each beam. Finally, the calculated sigma-0 values are encoded as digital serial data that emulates the IWRAP output data file. For each frequency, there are four parallel output streams, one for each band, which are 30 deg H & V pol, and 40 deg H & V pol.

In a real backscatter measurement there will always be instrument noise, which is simulated here by adding random Gaussian noise to the output sigma-0 data stream. The noise added is a Gaussian random variable with zero mean and standard deviation equal to a typical

value of 30% of the mean measured value. Table 5.1 shows a sample of serial data output from one of the streams.

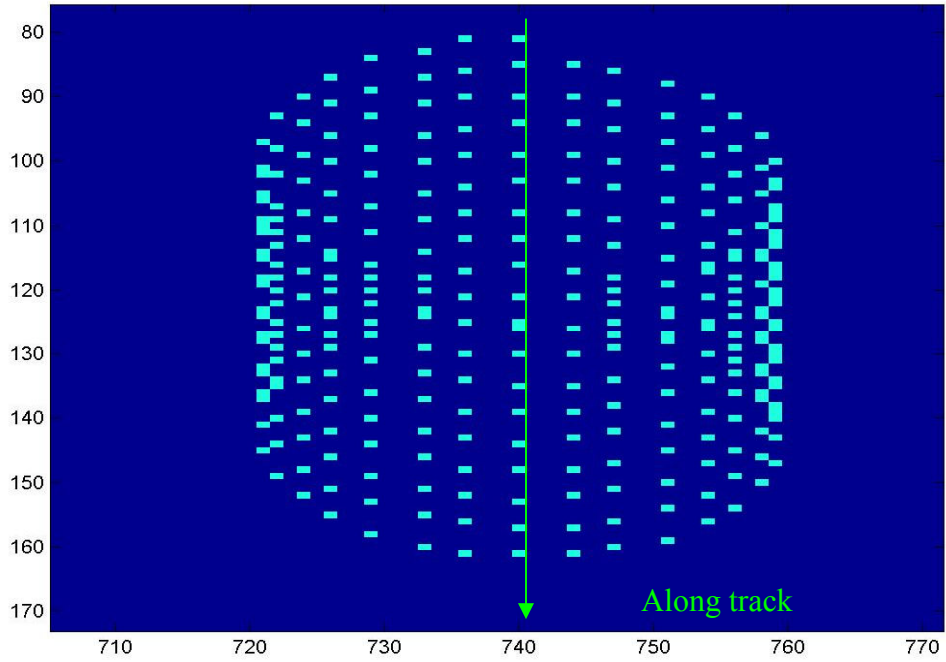


Figure 5.2 Antenna footprint center locations during conical scans.

Table 5.1 Sample of output serial data record.

Long index	Lat index	Incidence angle(deg)	Azimuth angle(deg)	Band 1=C band 2=Ku band	Pol 1=V pol 2=H pol	Sig-0 (dB)	Aircraft wind dir (deg)
982	132	40	5.625	1	2	-7.4164	64.353
986	133	40	16.875	1	2	-7.978	64.852
989	134	40	28.125	1	2	-6.8785	65.245
992	136	40	39.375	1	2	-7.2707	65.75
995	139	40	50.625	1	2	-7.3559	66.376
997	142	40	61.875	1	2	-7.7862	66.915
998	145	40	73.125	1	2	-7.5134	67.353
999	149	40	84.375	1	2	-7.3539	67.908
999	153	40	95.625	1	2	-7.6237	68.346
998	157	40	106.88	1	2	-7.7957	68.655

The wind vector retrieval algorithm was designed to use flight-level wind measurements from the aircraft inertial navigation system, as the reference wind direction. Because wind direction can change with altitude, it was necessary to incorporate this effect for the simulated aircraft measured wind direction. For this purpose, a systematic bias error was added to the corresponding surface wind direction, which was ± 30 deg peak difference, according to the distance from the eye of the hurricane. As shown in Fig. 5.3, this wind direction adjustment follows a sine wave that has a minimum near the center of the hurricane eye. This wind direction error is estimated to bound the possible changes that could occur with actual flight data.

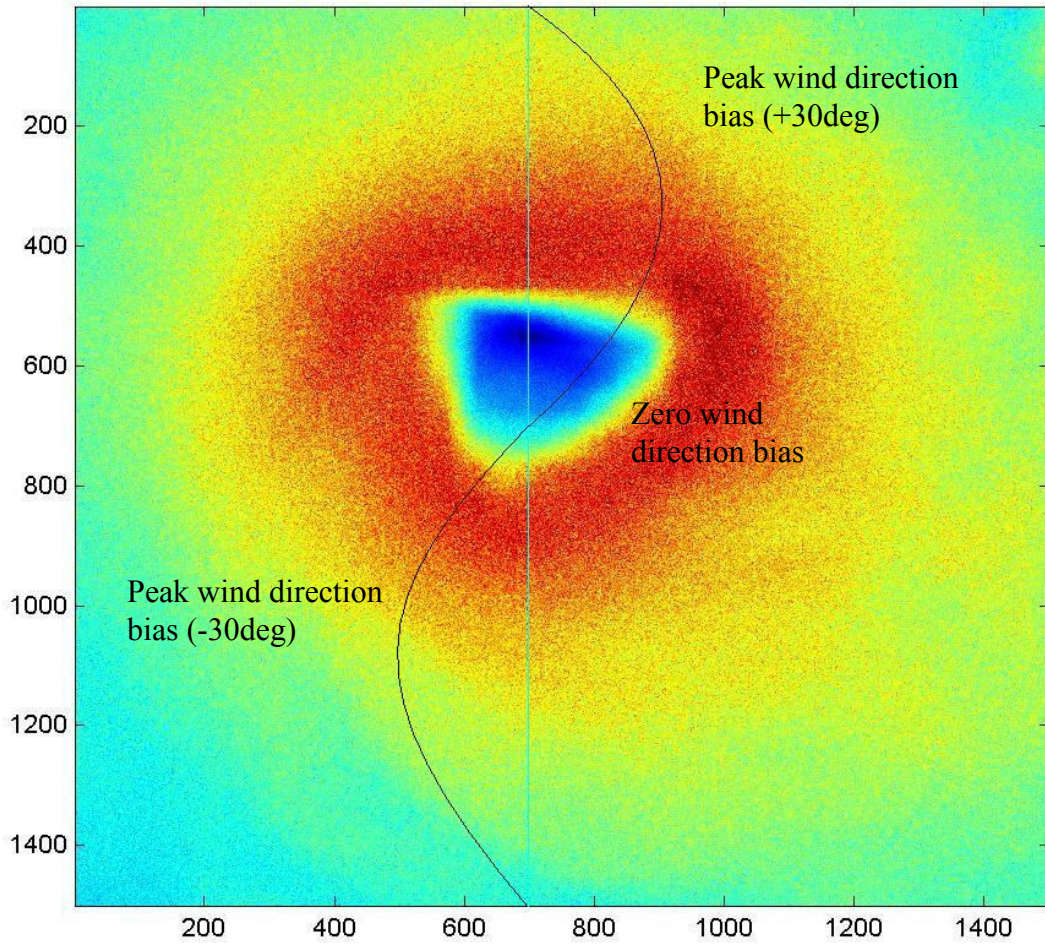
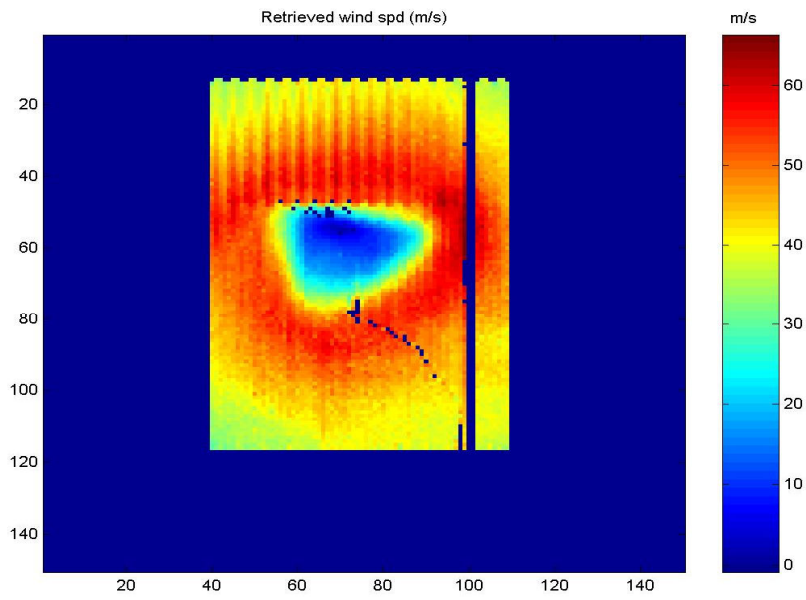


Figure 5.3 Wind direction bias added to simulate flight level wind direction measurement.

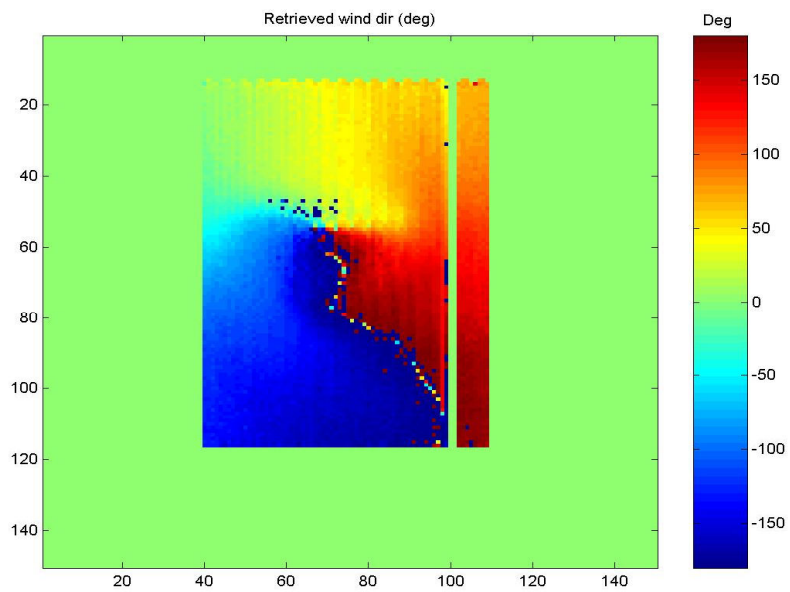
5.2 Results from Simulation

With the Monte Carlo simulation described above, seventeen simulated flight tracks were conducted over the hurricane and wind vectors were retrieved using the retrieval algorithm. Figure 5.4 shows the image of retrieved wind speed and direction values in 1 km x 1 km pixels from the simulated aircraft passes over hurricane Floyd. The occasional blue pixels are locations where the algorithm failed to retrieve a wind vector solution, which is attributed to extreme values of the simulated noise.

The retrieved values were then compared the original surface wind field and Fig. 5.5 shows the histogram of difference between measured and true value on a pixel by pixel basis. In total there were about 7000 pixels from all seventeen passes, and the mean difference in wind speed was found to be 0.8 m/s and the standard deviation was 2.2 m/s. Similarly, the mean difference in wind direction was 0.67 deg and the standard deviation was 12.7 deg. Close to zero values of the mean and reasonably low values of standard deviations indicate good simulation results.

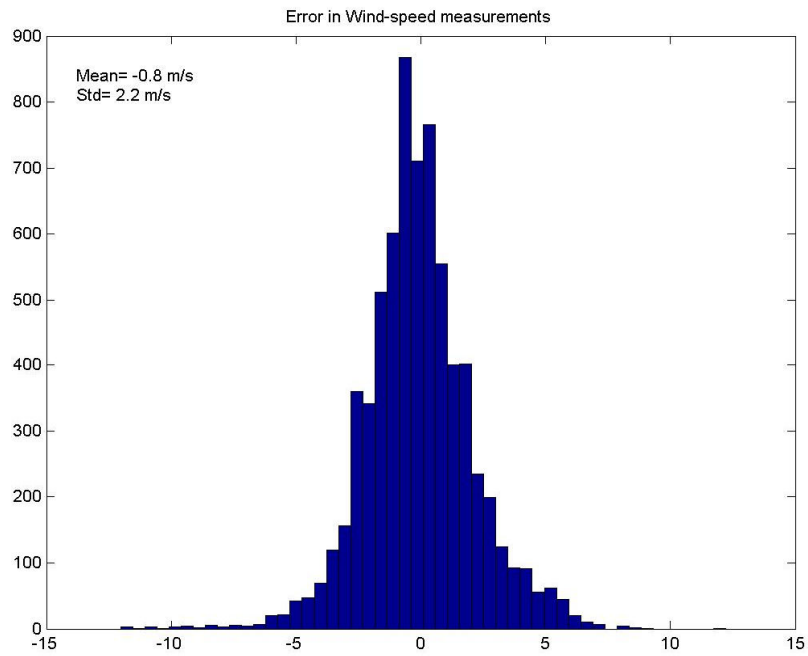


a. Wind speed retrievals.

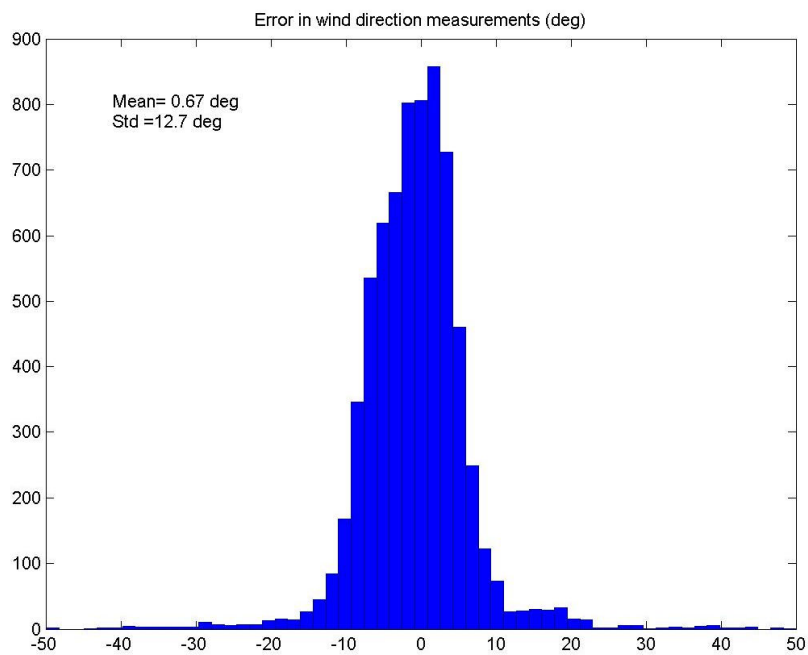


b. Wind direction retrievals.

Figure 5.4 Monte Carlo simulated results for hurricane Floyd.



a. Measured minus true wind speeds.



b. Measured minus true wind directions.

Figure 5.5 Analysis of pixel by pixel error in simulated hurricane.

Further, to understand the correlation between the measured and true winds, scatter plots were generated for wind speeds and directions; and the plots are presented in Figs. 5.6 and 5.7. It may be noted that most points in the wind speed plot lie in the range of 40 to 60 m/s, which is typical of a hurricane; and most points lie along the 45 deg line of agreement. In the case of wind direction, the few points far from the 45 deg line of agreement may be because of the selection of the wrong alias. In all, the statistics show that the wind retrieval algorithm has worked well.

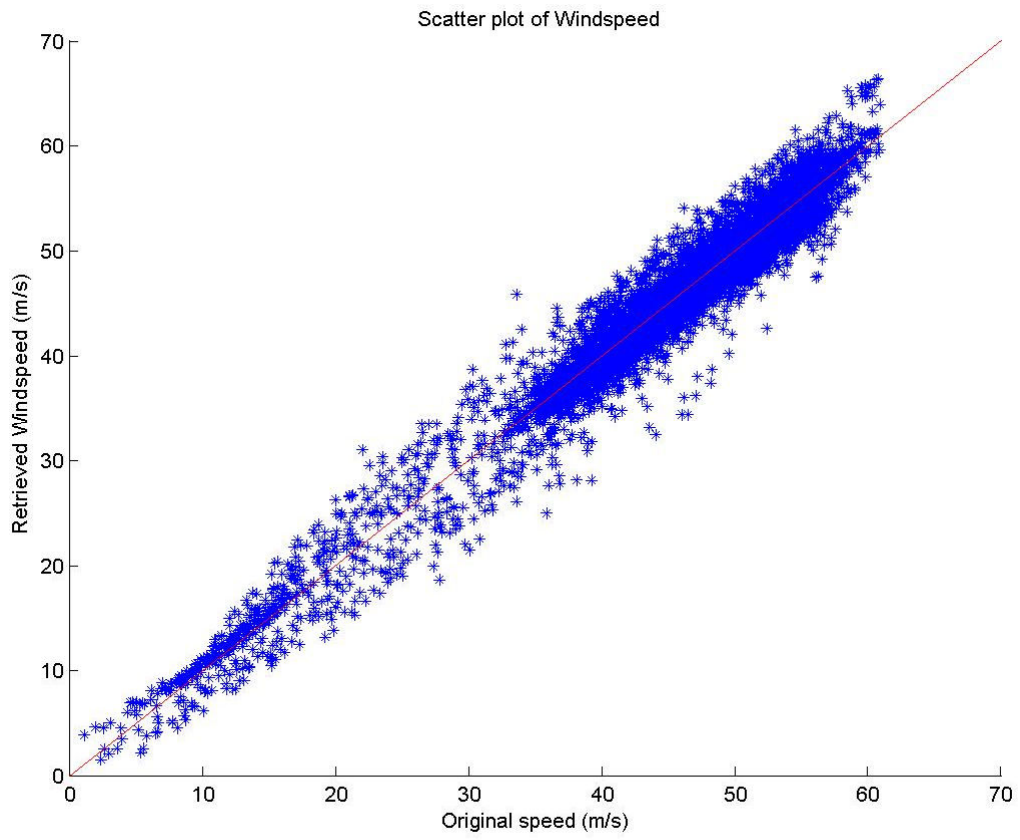


Figure 5.6 Scatter plot of wind speeds.

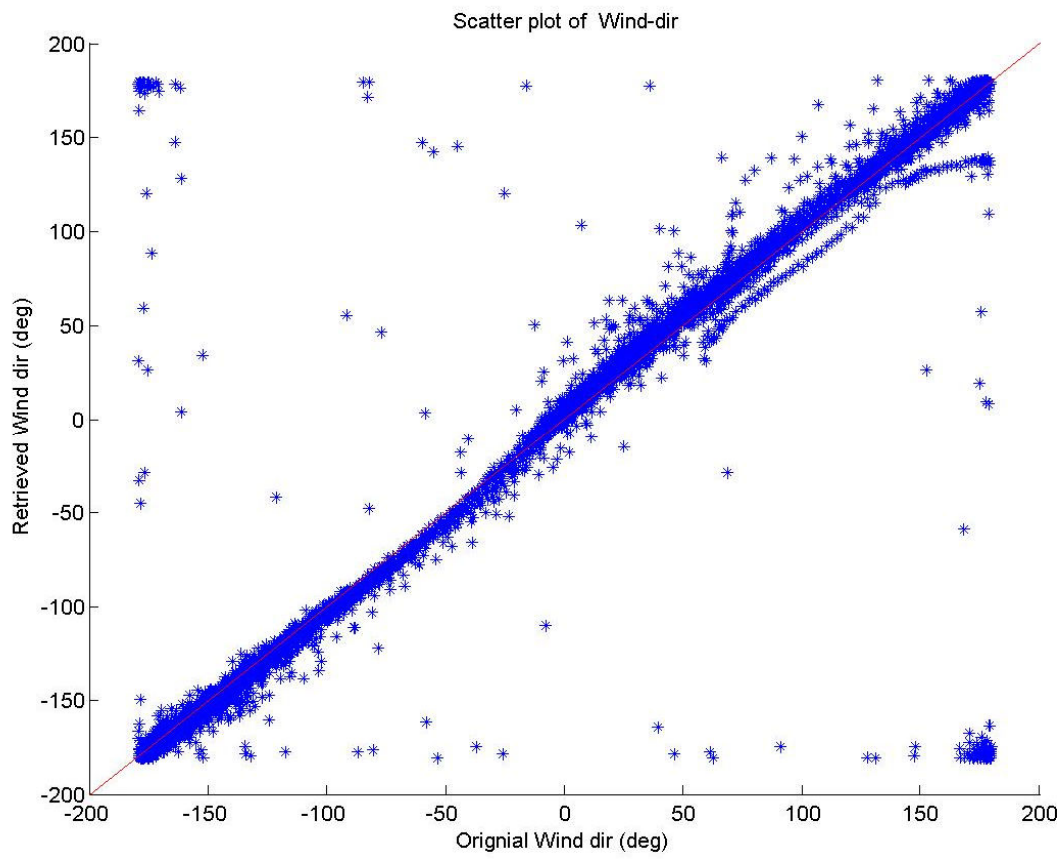


Figure 5.7 Scatter plot of wind directions.

CHAPTER 6: CONCLUSIONS

The objective of this thesis was to develop an accurate wind retrieval algorithm that operates fast enough for real-time retrieval that can be used to process hurricane wind data from the IWRAP airborne conically scanning scatterometer measurements of ocean surface backscatter. Unfortunately, actual flight data from IWRAP were not available as originally envisioned; but simulated data were used to validate that all specifications were fully met.

Chapter 4 describes the design of the algorithm and the techniques used to improve the computational efficiency to achieve real-time processing. Performance tests demonstrated faster than real-time data processing using simulated IWRAP measurements. These scatterometer sigma-0 measurements from the NOAA WP3 aircraft were simulated using a Monte Carlo technique (to add realistic instrument noise) and a numerical weather model hurricane wind field. Wind speed and direction retrieval performance were validated and results are provided in chapter 5. Using realistic values of measurement noise, the retrieved vectors fully met the measurement requirements including wind vector accuracy and real-time processing using standard PC's running MatLab scripts (see Appendix A). Further optimization using a compiled language such as FORTRAN will result in significantly faster than real-time operation.

APPENDIX
SIMULATION CODE

Each of the files below requires the appropriate input data files; which are processed data according to the flight parameters and are selectable. The main file that performs the retrieval is “o5retrieve.m”. Files that perform the Monte Carlo simulation of actual hurricane sigma-0 measurement by the scatterometer are:

- o1pregeo.m
- o2geo_sig_rev2.m
- o3colocate_rev4.m
- and o4avrg_rev2.m

The m-file script, “o1pregeo.m” uses hurricane wind field data that is provided by HRD in the form of U & V vectors. It interpolates these wind components to 1 km x 1 km WVC’s and converts the data into speed and direction format. The m-file “o2geo_sig_rev2.m” takes the wind field data generated by “o1pregeo.m” and calculates the sigma-0 for each WVC using the GMF and adds Gaussian noise. The m-file “o3colocate_rev4.m” collocates sigma-0 measurements for different scanning beams; and the m-file “o4avrg_rev2.m” checks for occurrence of more than one similar measurement within a WVC and averages them, if any.

Finally, the m-file “o5retrieve.m” implements the wind retrieval algorithm for each WVC using the sigma-0 data generated by the simulation codes. It uses the m-file “sigma02_mle.m” to generate sigma-0’s using GMF, and the m-file “localmin2.m” to search for the local minima on the cost surface.

The following are MatLab scripts (m-files) developed in this thesis:

o1pregeo.m

```
clear
load('C:\Work\IWRAP\miami\1999091312.mm5.mat')
%win=sqrt(UN10.^2+VN10.^2);

u=UN10(161:190,481:510);
v=VN10(161:190,481:510);

u1 = imresize(u,050,'bilinear');
v1 = imresize(v,050,'bilinear');

UN10_2=u1*0.1;
VN10_2=v1*0.1;
noise=randn(1500,1500);
fi_n=noise.*UN10_2;
fi_v=noise.*VN10_2;
u1=fi_n+u1;
v1=fi_v+v1;

% uu=reshape(u,1,30*30);
% vv=reshape(v,1,30*30);
% sd1=abs(0.03*mean(uu));
% sd2=abs(0.03*mean(vv));
%
% noise=normrnd(0,sd1,1500,1500);
% noise1=normrnd(0,sd2,1500,1500);
%
% u1=u1+(u1.*noise);
% v1=v1+(v1.*noise1);

spd=sqrt(u1.^2+v1.^2);
dir=(180/pi).*atan2(v1,u1);

spd(spd>65)=65 ;

% dir(u1>0 & v1>0)=-dir(u1>0 & v1>0);
% dir(u1<0 & v1<0)=dir(u1<0 & v1<0)+90;
% dir(u1>0 & v1<0)=180+dir(u1>0 & v1<0);
% dir(u1<0 & v1>0)=90+dir(u1<0 & v1>0)+270;
```

```
save spd_dir spd dir
```

```
% a=0;  
% for i=1:50:1500  
%   a=a+1;  
%   b=0;  
%   for j=1:50:1500  
%     b=b+1;  
%     u2(a,b)=u1(i,j);  
%   end  
% end  
% end
```

o2geo_sig_rev2.m

```
clear  
load spd_dir  
load p1;  
%w=zeros(1500,1500);  
%w=spd;  
cd C:\Work\IWRAP\windr  
record=zeros(0,8);  
ad=zeros(1500,3);  
ad(:,1)=linspace(0,360,1500)';  
ad(:,1)=ad(:,1)*pi/180;  
ad(:,2)=sin(ad(:,1));  
ad(:,3)=ad(:,2)*10;  
  
%p1=439;  
p2=150;  
xf(1)=p1;  
yf(1)=p2;  
  
c=-3.90625;  
i=0;  
q=0;  
for rev=1:800  
  
for theta=(11.25/2):11.25:360  
    j=0;  
    i=i+1;  
    c=c+3.90625;  
    xf(i)=xf(1);  
    yf(i)=yf(1)+c;
```

```

yf1(i)=p2+round(((yf(i))-100)/100);

th=(90+theta)*pi/180 ;
q=q+1;
for r=[1320 1918]
    x=r*-cos(-th);
    y=r*sin(-th);
    if r==1320
        inc=30;
        X1(i)=round((x/100)+xf(i));
        Y1(i)=round((y/100)+yf1(i));
        U=spd(Y1(i),X1(i));
        D=dir(Y1(i),X1(i));
        X=[theta-D] ;
        band =[1];
        for pol=[1 2]
            j=j+1 ;
            si=gmf1(U,X,inc,band,pol);
            sigm=10*log10(si);
            sigma1=[X1(i) Y1(i) inc X+D band pol sigm D+ad(Y1(i),3)];
            if sigma1(1,6)==1
                record30V(q,:)=sigma1(1,:);
            end
            if sigma1(1,6)==2
                record30H(q,:)=sigma1(1,:);
            end
        end
    end
end
if r==1918
    inc=40;
    X2(i)=round((x/100)+xf(i));
    Y2(i)=round((y/100)+yf1(i));
    U=spd(Y2(i),X2(i));
    D=dir(Y2(i),X2(i));
    X=[theta-D] ;
    band =[1];
    for pol=[1 2]
        %j=j+1 ;
        si=gmf1(U,X,inc,band,pol);
        sigm=10*log10(si);
        sigma1=[X2(i) Y2(i) inc X+D band pol sigm D+ad(Y2(i),3)];
        if sigma1(1,6)==1
            record40V(q,:)=sigma1(1,:);
        end
    end
end

```

```

        if sigma1(1,6)==2
            record40H(q,:)=sigma1(1,:);
        end
    end
end
end
end
s=size(record,1);
% record(s+1:(s+3+1),:)=sigma1(1:4,:);
end
dim=i;
end

```

```

m1=abs(0.03*mean(record30H(:,7)));
m2=abs(0.03*mean(record30V(:,7)));
m3=abs(0.03*mean(record40H(:,7)));
m4=abs(0.03*mean(record40V(:,7)));
si=size(record30H,1);
noise1=normrnd(0,m1,si,1);
noise2=normrnd(0,m2,si,1);
noise3=normrnd(0,m3,si,1);
noise4=normrnd(0,m4,si,1);
record30H(:,7)=record30H(:,7)+noise1;
record30V(:,7)=record30V(:,7)+noise2;
record40H(:,7)=record40H(:,7)+noise3;
record40V(:,7)=record40V(:,7)+noise4;

```

```
cd C:\Work\IWRAP\miami
```

```
save record record30H record30V record40H record40V xf yf yf1
```

```

% w=zeros(1500,1500);
% for j=1:size(Y2,2)
%     w(Y2(j),X2(j))=100;
% end
% figure,imagesc(w)

```

o3colocate_rev4.m

```

clear
load record
z=cell(150,150);
zz=zeros(150,150);
s=size(record30H,1);
cnt=0;

```

```

q=0;
%qq=0
for rev=0:32:s-32
    q=q+1;

    for st=1:32
        r=rev+st;
        x30=floor(record30H(r,1)/10);
        y30=floor(record30H(r,2)/10);

        x40=floor(record40H(r,1)/10);
        y40=floor(record40H(r,2)/10);

        ss=size(z{y30,x30},1);
        temp=z{y30,x30};
        temp(ss+1,:)=record30V(r,:);
        temp(ss+2,:)=record30H(r,:);
        z{y30,x30}=temp;
        zz(y30,x30)=zz(y30,x30)+2;

        ss=size(z{y40,x40},1);
        temp=z{y40,x40};
        temp(ss+1,:)=record40V(r,:);
        temp(ss+2,:)=record40H(r,:);
        z{y40,x40}=temp;
        zz(y40,x40)=zz(y40,x40)+2;
    end
end

%clear x* y*
save coloc z zz

```

o4avrg_rev2.m

```

clear
load coloc
z1=cell(150,150);
f=find(zz~=0);
for j=1:size(f,1)
    a=z{f(j)};
    b=sortrows(a,[3 4 6]);
    c=zeros(0,8);
    si=size(b,1);

```

```

tmp=b(1,:);
count=1;
for i=2:si
    if b(i,4)==b(i-1,4)&&b(i,6)==b(i-1,6)
        tmp=tmp+b(i,:);
        count=count+1;
    else
        c(size(c,1)+1,:)=tmp./count;
        tmp=b(i,:);
        count=1;
    end
end
c(size(c,1)+1,:)=tmp./count;
z1 {f(j)}=c;
end

save feild z z1 zz

```

o5retrieve.m

```

clear
load parameters
cd C:\Work\IWRAP\miami
load feild
load coloc
load spd_dir
spd1= imresize(spd,0.1,'bilinear');
dir1= imresize(dir,0.1,'bilinear');

% spd1=spd1';
% dir1=dir1';

cd C:\Work\IWRAP\windr

speed1=zeros(150,150);
direction1=zeros(150,150);

hs=60;% swath of cost fn around dir

x=0;
f=find(zz~=0);
%d=1:size(f,1)
for d=1:1
    sigma1=z1 {f(d)};

```



```

sol1=s1a(:,2);
sol1(isnan(sol1))=0;

s2=[mle sol2];
s2(s2==0)=nan;
s2a=sortrows(s2);
sol2=s2a(:,2);
sol2(isnan(sol2))=0;

idx1 = sol1(1);
idx1=idx1(idx1~=0);% 4 was 2

mark= 180+airD-hs;
if mark>361
    mark=mark-361;
end
idx1=(2*idx1)-1;
idx1=idx1+mark;
if idx1>361
    idx1=idx1-361;
end

if idx1<0
    idx1=361+idx1;
end

idx2 = sol2(1:2);
mle_value = wind_vec(1:2,3);

ret_dir=nan;
ret_spd=nan;

ret_dir(find(idx1)) = direction(idx1(find(idx1))); % (+180 to convert to wind flow directions)

ret_spd(find(idx2)) = guess_spd+speed(sol2(find(idx2)));
ret_spd(find(idx2)) = ret_spd(fliplr(find(idx2)));

speed1(f(d))=ret_spd(1);
direction1(f(d))=ret_dir(1);
end

cd C:\Work\IWRAP\miami
load windspd2

```

```

load winddir2
windspd2=windspd2+speed1;
winddir2=winddir2+direction1;
save windspd2 windspd2
save winddir2 winddir2
save result speed1 direction1

```

localmin2.m

```

%
=====
===
% Calculate local minima of the mle surface
%
=====
===
function [sol1,sol2,mle,k] = localmin(cost,s)

% cost(362:372,:)=cost(1:11,:);
% cost(:,82:92)=cost(:,1:11);

wsize1 = 11; % even numbers; x axis (wind speed)
wsize2 = 11; %even number; y axis (wind direction)
sol1 = zeros(15,1);
sol2 = zeros(15,1);
mle = zeros(15,1);
k = 0;

for j=1+(wsize1-1)/2:41-(wsize1-1)/2
    for i=1+(wsize2-1)/2:s-(wsize2-1)/2 % was 361 initially
        wins = cost(i-((wsize2-1)/2):i+((wsize2-1)/2),j-((wsize1-1)/2):j+((wsize1-1)/2));
        loc = find(wins == min(min(wins)));

        if loc == ((wsize1*(wsize2-1)/2+(wsize1-1)/2)+1)
            k=k+1;
            sol1(k)=i;
            sol2(k)=j;
            if j>81 % to avoid exceeding speed matrix
                sol2(k)=81;
            end
        end
    end
end

```

```

        mle(k) = cost(sol1(k),sol2(k));
    end
end
end
end

```

sigma02_mle.m

```

function cost = sigma0_mle(inc,speed,sig,azi,sig_var,pol,band,airD,hs)
sig = 10^(sig/10); %Convert dB to ratio
cost = zeros(1,361);
U=speed;

%*****

chi = linspace(-180,180,361);
direction = azi-chi;

id1 = find(direction > 180);
id2 = find(direction < -180);

direction(id1) = direction(id1)-360;
direction(id2) = direction(id2)+360;

p=[direction;1:361];
b=sortrows(p');

drc=linspace(-180,180,361);
drc=drc';
drc = drc(b(:,2));

m=[drc drc drc];
drc=m(361+181+airD-hs:361+181+airD+hs);
ss=size(drc,2);
drc=drc(1:2:ss);

%*****
model = gmfl(U,drc,inc,band,pol); % 000
sig_var = 2e-7; % change sigma0 standard deviation here!
cost = (1.0)*( (sig-model).^2/sig_var );
%figure,plot(cost,','),grid

```

LIST OF REFERENCES

- [1] F. T. Ulaby, R. K. Moore, and A. K. Fung, *Microwave Remote Sensing Active and Passive*, Vol 2, *Radar Remote Sensing and Surface Scattering and Emission Theory*. Reading: Addison-Wesley, 1982.
- [2] Richard K. Moore and W. Linwood Jones, "Satellite Scatterometer Wind Vector Measurement - the Legacy of the Saesat Satellite Scatterometer, IEEE GeoSci Rem Sens Newsletter, Issue-321, Sept. 2004
- [3] Jones, W. L., Schroeder, L. C., and Mitchell, J. L., "Aircraft Measurements of the Microwave Scattering Signature of the Ocean", *IEEE Trans. Ant & Prop/IEEE J. Oceanic Eng.* (Special Issue on Radio Oceanography), Vol. AP-25, No. I, pp 52-61, January 1977.
- [4] Moore, R. K. and A. K. Fung, "Radar determination of winds at sea," *Proc. IEEE*, vol. 67, pp. 1504-1521., 1979.
- [5] Naderi, F. M., M. H. Freilich, and D. G. Long, "Spaceborne radar measurement of wind velocity over the ocean--An overview of the NSCAT scatterometer system," *Proc. IEEE*, vol. 79, pp. 850-866, 1991.
- [6] Offiler, D., "The calibration of ERS-1 satellite scatterometer winds," *J. Atmos. & Oceanic Tech.*, vol. 11, pp. 1002-1017, 1994.
- [7] Plant, W.J. A two-scale model of short wind-generated waves and scatterometry. *Journal of Geophysical Research*, vol. 91, no. C9, pp. 10735-10749, 1986.
- [8] Schroeder, L. C., Boggs, D. H., Dome, G., Halberstam, I. M., Jones, W. L., Pierson, W. J. and Wentz, F. J., "The Relationship Between Wind Vector and Normalize Radar Cross

- section Used to Derive SeaSat-A Satellite Scatterometer Winds", *Journal of Geophysical Research*, Vol. 87, No. C5, pp 3318 - 3336, April 30, 1982.
- [9] Carswell, J.R., Carson, S.C., McIntosh, R.E. et al. Airborne scatterometers: investigating ocean backscatter under low- and high-wind conditions. *Proceedings of the IEEE*, vol. 82, no.12, pp. 1835-1860, 1994.
- [10] Yueh, S. H., et al., "QuikSCAT Geophysical Model Function For Tropical Cyclones and Application to Hurricane Floyd," *IEEE Trans. on Geosc. and Remote Sensing*, vol. 39, pp. 2601-2612, 2001.
- [11] Hersbach, H. (2003), An improved geophysical model function for ERS C-band scatterometry, ECMWF Technical Memorandum No. 395.
- [12] Katsaros, K., Forde, E., Chang, P., and Liu, W., QuikSCAT facilitates early identification of tropical depressions in 1999 hurricane season, *Geophysical Research Letters*, 2000.
- [13] Isaksen, L. and Stoffelen, A. (2000), ERS scatterometer wind data impact on ECMWF's tropical cyclone forecasts, *IEEE Transactions on Geo-science and Remote Sensing*, 38 (4):1885–1892.
- [14] Stoffelen, A. and Anderson, D. (1997), Scatterometer data interpretation: Estimation and validation of the transfer function cmod4. *Journal of Geophysical Research*, 102: 5767–5780.
- [15] Donnelly, W., Carswell, J., McIntosh, R., Chang, P., Wilkerson, J., Black, P., and Marks, F. (1999), Revised ocean backscatter models at c and ku-band under high wind conditions, *Journal of Geophysical Research*, 104(C5):11485–11497.

- [16] D. E. Fernandez, J. R. Carswell, S. Frasier, P. S. Chang, P. G. Black, F. D. Marks, “Dual Polarized C-and Ku- band Ocean Backscatter Response to Hurricane Force Winds”, *Journal of Geophysical Research* vol 104, No.C5, 1999.
- [17] D. E. Fernandez, E. M. Kerr, A. Castells, J. R. Carswell, S. J. Frasier, P. S. Chang, P. G. Black, F. D. Marks, “IWRAP: the Imaging Wind and Rain Airborne Profiler for Remote Sensing of the Ocean and the Atmospheric Boundary Layer within Tropical Cyclones”. *IEEE Trans. Geosci. Rem Sens*, vol. 43, No 8, 2005
- [18] Jean Yves Kabore, Linwood W Jones, Robbie Hood, Mark James and Frank LaFontaine, An Incidence Angle Correction for a Conical Scanning Microwave Radiometer, *IEEE South East Conference*, April 8-10, 2005, Ft Lauderdale, FL
- [19] Jones, W., Cardone, V., Pierson, W., Zec, J., Rice, L., Cox, A., and Sylvester, W. (1999), NSCAT high-resolution surface wind measurements in typhoon violet, *Journal of Geophysical Research*, 104(5): 11247–11259.